CXCR2 expression during melanoma tumorigenesis controls transcriptional programs that facilitate tumor growth

[*1,2] Yang J,[*1,2] Bergdorf K,[*1,2] Yan C, [1,2]Luo W, [3]Chen SC, [3]Ayers D, [3]Liu Q, [3]Liu X, [1,2,4]Boothby M, [5]Groves SM, [2]Oleskie AN, [6] Zhang X, [7]Maeda DY, [7]Zebala JA, [1,2]Quaranta V, [1,2] Richmond A**

[1]TVHS Department of Veterans Affairs, [2]Department of Pharmacology, [3]Department of Biostatistics, [4] Department of Pathology, Microbiology and Immunology, [5] Department of Biochemistry, Vanderbilt University School of Medicine, Nashville, TN 37232

[6] Department of Genomic Medicine, MD Anderson Cancer Center, University of Texas, Houston, TX 77030

[7] Syntrix Pharmaceuticals, Auburn, WA 98001

*These authors contributed equally to this manuscript

**Corresponding author ann.richmond@vanderbilt.edu

Abstract:

Though chemokine receptors are known to play a key role in cancer growth and response to therapy, a direct link between expression of a chemokine receptor in the tumor progenitor cell during induction of tumorigenesis has not been established**.** Here we addressed this key question in reference to a role for CXCR2 in melanoma tumorigenesis by generating tamoxifen-inducible tyrosinase-promoter driven *Braf*^{V600E}*/Pten*$^{-/-}$*/Cxcr2*$^{-/-}$ and *NRas*^{Q61R}*/INK4a*$^{-/-}$*/Cxcr2*$^{-/-}$ murine models of melanoma. Loss or pharmacological inhibition of CXCR2 in these models during tumor induction significantly reduced tumor size and incidence and promoted anti-tumor immunity. RNAseq analysis of tumors developing after melanocytic deletion or inhibition of CXCR2 revealed a novel mechanism for CXCR2 in melanoma tumorigenesis. The single gene that was significantly induced with a $\log_2$ fold change greater than 2 in three different melanoma models after CXCR2 ablation was *TFCP2L1*, a key tumor suppressive transcription factor. Moreover, CXCL1 activation of CXCR2 in melanocytes induced expression of genes normally suppressed when TFCP2L1 is high and this could be overcome by inhibition of CXCR2. Thus, during tumorigenesis, CXCR2 represses the expression of *TFCP2L1* which in turn is a global regulator of genes involved in growth regulation and tumor suppression, stemness and differentiation, and immune modulation.

Keywords: melanoma, CXCR2, tumor immune microenvironment, genomic analysis, genetic mouse models

Introduction

Chemokines and their receptors have been shown to play an essential role in regulating tumor growth, progression, metastasis, and response to immunotherapy (Hanahan, 2022; Moser, 2022; Singh et al., 2009a; Vandercappellen et al., 2008). Though chemokines were initially identified as chemoattractants used to guide leukocyte migration, there has been increasing evidence that they can regulate other functions in a broader array of cell types, including cancer cells (Raman et al., 2011) (for review).

The CXCR1/CXCR2 ligand-receptor axis has been widely characterized as a driver of aggressive behavior in many cancer types, including breast, prostate, melanoma, lung, colorectal, pancreatic, and renal cancers (Cheng et al., 2021; Ha et al., 2017; Liao et al., 2019; Luan et al., 1997; Romero-Moreno et al., 2019; Ruffini, 2019; Singh et al., 2013; Singh et al., 2009a). CXCR1/CXCR2 ligands, including CXCL1-3, 5-8 are produced by endothelial cells, tumor-associated macrophages, cancer-associated fibroblasts, adipocytes, and cancer cells (Ha et al., 2017). These CXCR1 and CXCR2 ligands play a significant role in the recruitment of neutrophils and myeloid-derived suppressor cells (MDSCs) to the tumor microenvironment (TME), both of which are associated with poor outcomes (Bullock &Richmond, 2021; Che et al., 2020; Yang et al., 2021). In addition to altering the tumor immune microenvironment, these chemokine ligands can also activate phosphatidylinositol-3-kinase (PI3K), phospholipase-Cβ, calcium mobilization, mitogen-activated protein kinase (MAPK), protein kinase B (AKT), transcription factors like NF-κB, and gene expression on tumor cells. These chemokine responses have

been linked to tumor cell survival, proliferation, migration, as well as angiogenesis (Addison et al., 2000; Ha et al, 2017; Hou et al., 2015; Sai et al., 2008; Shang & Li, 2019).

Many cancer cells exhibit induction or increased expression of multiple ligands for both CXCR1 (CXCL1-3, 5-8) and CXCR2 (CXCL1-3, 5 and 7). Moreover, CXCR1 and CXCR2 are differentially expressed in human tissues, though in mouse, CXCR2 is the predominant receptor mediating response to the murine chemokine ligands during inflammation, angiogenesis, and tumor growth (CXCL1,2,3 and 5, also known as KC, MIP2α, MIP2β, and LIX) (Fan, 2007; Moepps, 2006, Moepps B, 2015). In addition to a function in the attraction of hematopoietic cells that influence the tumor microenvironment and tumor progression, it has been suggested that these receptors may exert autocrine effects on tumor growth. In the case of melanoma, mouse xenograft models provide compelling evidence that tumor cells take advantage of CXCR2 ligand expression to either suppress the anti-tumor immune response or to induce tumor growth and angiogenesis and alter the TME and facilitate metastasis (Araki et al., 2007; Balentien et al., 1991; Richmond et al., 1988; Richmond et al., 2009; Romero-Moreno et al., 2019; Ruffini, 2019; Singh et al., 2007; Singh et al., 2009a; Singh et al., 2010; Yang & Richmond, 2001, Yang et al., 2009).The CXCR1/CXCR2 signaling nexus directly influences the sensitivity of tumor cells to chemotherapies by altering pathways associated with apoptosis and multidrug resistance (Shi et al., 2012; Wilson et al., 2008), resulting in a poor prognosis in human cancer studies (Balasoiu et al., 2014; Pine et al., 2011). The past decade has witnessed the generation and development of antagonists to CXCR1 and CXCR2, and multiple clinical trials are

underway investigating the therapeutic potential of targeting this signaling axis in inflammatory disorders and cancers (NCT03161431, NCT04245397, NCT03400332) (Bertini et al., 2004; Casilli et al., 2005; Chapman et al., 2009; Hunt et al., 2007; Leaker et al., 2013; Maeda et al., 2014; Maeda et al., 2010; Souza et al., 2004).

We previously demonstrated that targeted deletion of CXCR2 in myeloid cells or systemic treatment with the CXCR1/CXCR2 antagonist SX-682 conferred anti-tumor immunity via reduction of MDSC infiltration into the TME and enhanced CD8+ T cell activation (Yang et al., 2021). However, it remains controversial as to whether there is a direct function of either or both CXCR1 and CXCR2 on the growth of the cancer cells, and if so, which of these receptors are involved and what mechanisms are employed. To clarify the concept of an autocrine role for CXCR2 and its ligands in melanoma progenitor cells, we used an inducible, autochthonous model of malignant melanoma in mice. Using two distinct modes of triggering the formation of malignant melanoma, we found that tumor onset, growth, and outcome accompanied changes in tumor microenvironment and gene expression when *Cxcr2* was deleted in melanoma precursor cells. Since over 75% of melanoma tumors exhibit *Braf* or *NRas* mutation, often with loss of tumor suppressors *Pten* or *Ink4a*, we examined the role of *Cxcr2* deletion in genetically engineered mouse (GEM) models of $Braf^{V600E}/Pten^{-/-}$ and $NRas^{G61R}/INK4a^{-/-}$ melanoma via a tyrosinase-inducible promoter/enhancer. We demonstrate that targeted deletion of *Cxcr2* in tyrosinase-expressing melanoma precursor cells concurrent with induction of the $Braf^{V600E}$ transgene and loss of *Pten* expression ($Pten^{-/-}$) (Dankort et al., 2007; Dankort et al., 2009; Liu et al., 2013) or induction of $NRas^{Q61R}$ and loss of *Ink4a* ($INK4a^{-/-}$)(Burd et al., 2014), resulted in a

significant reduction of melanoma burden. Importantly, we also observed altered gene expression and promotion of an anti-tumor immune environment when CXCR2 was deleted in tyrosinase-expressing melanoma precursor cells during transformation in these mouse models as compared to models with intact tumor cell expression of CXCR2. Moreover, we show that the CXCR1/CXCR2 antagonist, SX-682, accomplishes a similar reduction in melanoma tumor burden, establishes an anti-tumor immune microenvironment, and significantly alters the transcriptional profile of melanoma cells when delivered during the transformation process. Remarkably, an analysis of common gene expression changes due to loss or inhibition of CXCR2 during tumorigenesis converged on one, but only one, gene -- the tumor suppressive transcription factor *TFCP2L1*. These data model a key mechanism for CXCR2 regulation of melanoma tumor growth through negative regulation of a transcription factor with tumor suppressive activity, *TFCP2L1.*

Results

CXCR2 Correlates with Poor Prognosis in Patient Populations and Response to Checkpoint inhibitors

Using the available Gene Expression Omnibus (GEO) cohort, we evaluated *CXCR1, CXCR2,* and *CXCL1-3, 5* and *8* (CXCR1/CXCR2 ligands) expression in nevi and melanoma. *CXCR1* and *CXCR2* mRNA exhibited a trend toward increased expression in melanoma compared to nevi, but these differences were not statistically significant (Figure 1A). However, C*XCL1*, *CXCL2*, *CXCL3*, *CXCL5* and *CXCL8* mRNAs were significantly upregulated in melanoma samples compared to benign nevi (Figure 1B).

Furthermore, there were no significant differences in *CXCR1* and *CXCR2* expression among nevi and melanoma tumors when stratified by *BRAF* or *NRAS* mutation status (Figure S1A, B). However, since the number of samples available for analysis of mutation status was small, these findings should be interpreted cautiously.

CXCR2 has been associated with increased tumor growth and poor prognosis across multiple cancers(Ha et al., 2017). To define the relationship between *CXCR2* expression and the clinical prognosis of melanoma patients, we examined clinical data from the Cancer Genome Atlas (TCGA), and the skin cutaneous melanoma (SKCM) dataset using Gene Expression Profiling Interactive Analysis (GEPIA). Survival analysis comparing patients with high *CXCR2* expression (n=114) to patients with lower *CXCR2* expression (n=107) indicates that *CXCR2* expression correlates with decreased overall survival of melanoma patients ($p=0.035$, Figure 1C). Evaluation of survival in a patient cohort treated with anti-PD-1 therapy also suggests that patients with high *CXCR2* expression (n=24) exhibited poor prognosis in response to anti-PD-1 when compared with patients with low *CXCR2* expression (n=23, $p<0.01$; Figure 1D) (Liu et al., 2019a). Finally, analysis of another immune checkpoint inhibitor-treated cohort showed that responding patients had significantly lower *CXCR2* expression than non-responders (Figure 1E, ($p<0.05$) (Riaz et al., 2017). These data indicate that *CXCR2* expression correlates with poor therapeutic response in melanoma patients.

CXCR2 Influences Tumor Differentiation Status and Enhances Tumor Growth

To evaluate the role of CXCR2 in *Braf*^{V600E}*/Pten*$^{-/-}$ melanoma tumorigenesis, we crossed the C57BL/6 *Tyr-CreER+::Braf*^{V600E}*/Pten*$^{fl/fl}$*::mT/mG::mouse* (*Braf*^{V600E}*/Pten*$^{-/-}$) (Dankort

et al., 2009) with C57BL/6 mice carrying a *Cxcr2*$^{fl/fl}$ *allele* (Liu et al., 2013) to produce *Tyr-CreER+::Braf*^{V600E}*/Pten*$^{fl/fl}$*::mT/mG::Cxcr2*$^{-/-}$ and *Tyr-CreER+::Braf*^{V600E}*/Pten*$^{fl/fl}$*::mT/mG::Cxcr2*^{WT} littermates. Four-week-old mice were treated with 4-OH tamoxifen (4HT) to induce the tyrosinase promoter-driven Cre-recombinase. The resulting melanoma tumors that developed over 36 days were counted and measured. We observed that tumor burden and incidence (Figure 2A-C) were significantly reduced in *Braf*^{V600E}*/Pten*$^{-/-}$ mice with melanocyte targeted deletion of *Cxcr2* (*Braf/Pten/Cxcr2*$^{-/-}$*)* (271±361mm^3, n=21) in comparison to *Braf*^{V600E}*/Pten*$^{-/-}$ mice expressing CXCR2 *(Braf/Pten/Cxcr2*^{WT}*)* (615±609mm^3, n=24, $p<0.05$). The tumor number per mouse was also reduced upon melanocytic *Cxcr2* deletion (0.7±0.9 vs. 2.1±2.3, $p<0.05$). These data indicate that the CXCR2 signal transduction pathway plays a role in the induction and growth of Braf^{V600E}/Pten$^{-/-}$ melanoma.

To determine whether *CXCR2* is also important in *Nras/Ink4a* melanoma tumors, we crossed the *Tyr-CreER+::NRas*^{Q61R}*/Ink4a*$^{-/-}$*::mT/mG::* mouse (Burd et al., 2014) mice with the *Cxcr2*$^{fl/fl}$ mouse (Liu et al., 2013). New-born pups (1-2 days old) were exposed to 4-HT, followed by ultraviolet (UV) irradiation on day 3, and tumor growth was evaluated over five months. We observed significantly reduced tumor volume with deletion of *Cxcr2* (360±285mm^3) when compared to *NRas/Ink4a Cxcr2*^{WT} mice (764±601mm^3) (Figure 2D-F, $p<0.05$, n=16). However, in contrast to the Braf^{V600E}/Pten$^{-/-}$ model, the number of tumors per mouse was not significantly different between *Cxcr2*$^{-/-}$ (1.69±1.08) and *Cxcr2*^{WT} mice (1.88±1.26, p=0.654). As the *NRas* GEM model requires UV irradiation in addition the genetic alterations, it is possible that UV irradiation induces additional oncogenic pathways that function independent of CXCR2.

To elucidate the mechanism by which CXCR2 perturbation in melanocytes could alter the initiation and growth of *Braf*^{V600E}*/Pten*$^{-/-}$ *(Braf/Pten)* melanoma, we examined the transcriptome of tumors arising in *Braf/Pten/Cxcr2*^{WT} (n=7) and *Braf/Pten/Cxcr2*$^{-/-}$ (n=8) mice. RNA sequencing (RNAseq) analysis of tumor mRNA identified altered expression of 6213 genes in *Braf/Pten/Cxcr2*$^{-/-}$ tumors when compared to *Braf*/*Pten/Cxcr2*^{WT} *tumors* (Figures 2G, S3A, S4). Interestingly, gene set enrichment analysis (GSEA) focused on differentiation and immune function revealed that loss of CXCR2 expression in *Braf/Pten* tumors resulted in a significant increase in expression of genes involved in CD4+ T cell activation and lymphocyte activation, with a trend toward increased leukocyte proliferation, immune response, and stem cell differentiation (Figure 2H). However, there is also a paradoxical change in genes involved in lymphocyte anergy. Figure S3A shows a heat map of significantly differentially expressed genes in *Braf/Pten* tumors expressing or not expressing CXCR2. Several genes were upregulated in *Braf/Pten/Cxcr2*$^{-/-}$ tumors, including those that are immune related, associated with stem cell differentiation, and those involved in tumor suppression. This gene analysis also revealed downregulation of genes involved in growth, proliferation, and cell cycle*;* immune-related genes; motility and cell adhesion; differentiation/stemness and tumor suppression (Figure S3A). Together, these RNA sequencing data imply that *Cxcr2*$^{-/-}$ tumors may become less cohesive/dense, with diminished invasive potential and growth signaling, as modeled by Eikenberry *et al.* (Eikenberry et al., 2009).

We next evaluated gene expression in reference to the top 20 oncogenes with reduced expression and the top 20 induced tumor suppressor genes based on their $\log_2$ fold change and $-\log_{10}$ p-value in association with loss of CXCR2 during tumorigenesis in

Braf/Pten mice. Several genes involved in growth were significantly downregulated (red arrows; Figure S4A), while genes associated with tumor suppression were upregulated (red arrows; Figure S4B). Genes in common in both enrichment analyses in Figure S3A and Figure S4 include upregulation of the tumor suppressors *Tmprss11e*, *Adamts18* and *Tgm3*, as well as induction of the pyroptosis regulating gene *GSDMc* and the epithelial-specific ETS transcription factor 1 (*Elf3*). Commonly down-regulated genes include activators of the lectin pathway of the complement system (*Fcna*), myosin light chain kinase 4 (*MLK4*), and pathogen recognition receptors (*Cd209*). These changes likely contribute to differences in tumor growth observed when CXCR2 is targeted in melanocytes during transformation.

CXCR2 Contributes to an Immunosuppressive Melanoma Tumor Microenvironment

While GSEA identified enrichment of stem cell and growth-associated gene sets in *Braf/Pten/Cxcr2*$^{-/-}$ mice, it also revealed induction of gene sets associated with CD4+ T cell activation, lymphocyte activation, and leukocyte proliferation (Figure 2H). These results prompted analysis of the immune cell infiltrate between *Braf/Pten/Cxcr2*^{WT} and *Braf/Pten/Cxcr2*$^{-/-}$ tumor-bearing mice. We first utilized the murine Microenvironment Cell Population counter (mMCPcounter, (Petitprez et al., 2020), an immune deconvolution algorithm developed for bulk murine RNA sequencing data. mMCPcounter predicted an increase in CD3+ T cells, CD8+ T cells, monocytes, lymphatic vessels, and eosinophils, as well as a decrease in mast cells and endothelial cells ($p<0.05$) (Figures 3A, S5A), suggesting enhanced anti-tumor immunity in the *Braf/Pten/Cxcr2*$^{-/-}$ TME. In contrast, there was a decrease in NK cells. To further

analyze the immune environment *in vivo*, we defined the profile of CD45+ cells from peripheral blood and tumor of *Braf/Pten/Cxcr2*^{WT} and *Braf/Pten/Cxcr2*$^{-/-}$ tumor-bearing mice using FACS analysis. In agreement with the mMCPcounter predicted leukocytic infiltrates, we observed that deletion of CXCR2 in melanocytes undergoing transformation skewed the TME toward anti-tumor immunity. FACS analysis of the CD45+ cells in the tumors of *Braf/Pten/Cxcr2*$^{-/-}$ mice revealed a decrease in the immunosuppressive Ly6G+CD11b+ ($p<0.01$) and CD14+ G-MDSC ($p<0.05$) cells with no change in total CD11b+ cells (Figure 3B), in addition to a trend toward decreased CD25^{hi}CD45+CD3+ regulatory T cells and a trend toward an increase in the frequency of CD3+CD8+T cells. There was also a significant increase in memory CD44+CD4+ T cells ($p<0.05$) and activated CD69+CD8+ T cells ($p<0.05$) within the *Braf/Pten/Cxcr2*$^{-/-}$ tumors (Figure 3C, S5D). FACS analysis of peripheral blood cells revealed with no significant change in any peripheral blood population (Figure S5B).

The identified differences in immune cell infiltrate are highly suggestive of altered cytokine signaling within the TME. Therefore, a 62-cytokine array was performed on *Braf/Pten/Cxcr2*^{WT} (n=4) and *Braf/Pten/CXCR2*$^{-/-}$ (n=4) tumor lysates. CCL20, an inflammatory chemokine that is highly chemotactic for CCR6-expressing lymphocytes and dendritic cells, is strongly upregulated (24-fold) in the *Braf/Pten/Cxcr2*$^{-/-}$ TME (Figure 3D). In addition, RNAseq analysis revealed a significant increase in PD-L1 expression in tumors from *Braf/Pten/CXCR2*$^{-/-}$ mice compared to *Braf/Pten/Cxcr2*^{WT} mice (Figure 3E). Furthermore, M-CSF, eotaxin, and MIP-2 were slightly increased, which could contribute to myeloid cell infiltration, and there was a slight decrease in IL-1β in the tumors from *Braf/Pten/Cxcr2*$^{-/-}$ mice as compared to tumors from

Braf/Pten/Cxcr2^{WT} mice (Figure S5C). These data suggest that targeted deletion of *Cxcr2* in melanocytes during tumorigenesis results in a marked increase in CCL20 and additional subtle changes in the cytokine milieu of the TME.

CXCR1/CXCR2 Antagonist SX-682 Inhibits *Braf*^{V600E}*/Pten*$^{-/-}$ and *NRas*^{Q61R}*/Ink4a*$^{-/-}$ Melanoma Tumor Growth and Promotes Anti-Tumor Immunity

Having established the importance of CXCR2 in the development, growth, and TME of *Braf/Pten* melanoma tumors, we sought to evaluate the therapeutic potential of systemic CXCR2 inhibition. Thus, chow containing the CXCR1/CXCR2 antagonist SX-682 (Sun et al., 2019) was administered to four-week-old mice. After two weeks of eating vehicle control or SX-682 containing chow, 4-HT was applied to the backs of the mice for three successive days. Following a month of continuous feeding on control or SX-682-containing chow, we observed that mice fed SX-682-containing chow exhibited a trend toward reduction in tumor volume compared to mice fed vehicle control chow (Figure 4A, p=0.07, 802.5±724.01mm^3 for control; 230.20±373.21mm^3 for SX-682). Moreover, there was a trend toward decreased tumor formation in SX-682-fed mice (p=0.145), where only 40% of SX-682-fed mice developed tumors compared to 75% of control-fed mice (Figure 4B). Similarly, *NRas*^{Q61R}*/Ink4a*$^{-/-}$ (*NRas/Ink4a)* mice were fed chow containing SX-682 or control chow, and tumors that developed over five months were collected, measured, and processed for flow cytometry or cytokine array analysis. We observed that SX-682 treatment significantly suppressed tumor growth (p=0.041, Figure 4C) but only trended toward a decrease in tumor incidence (p=0.111, Figure 4D).

RNA sequencing analysis of control and SX-682 treated tumors from *Braf/Pten* mice identified nearly 3000 differentially expressed genes with many trends similar to those observed in *Braf/Pten/Cxcr2*$^{-/-}$ tumors. A volcano plot shows that a significant number of genes were strongly up or down-regulated ($\log_2$ fold change of > 3) with a very high level of significance ($-\log_{10}$(P-adj)>50) (Figure 4E). Upregulated genes include those involved in the following processes: regulation of growth, proliferation, and cell cycle*;* tumor suppression*;* differentiation/stemness; immune regulation; and motility and adhesion. Genes downregulated in response to CXCR1/CXCR2 antagonism with SX-682 include those involved in cell adhesion and cell proliferation, cell cycle and growth (Figure S3B).

GSEA of the tumors from *Braf/Pten* mice treated with SX-682 revealed significant increases in CD8+ T cell activation, with trends toward increased T cell-mediated immune response to the tumor, immune response to tumor, adaptive immune response, antigen processing and presentation, CD4+T cell activation, stem cell differentiation, CD8+ T cell proliferation, T cell-mediated cytotoxicity, and lymphocyte activation. There were significant decreases in genes involved in melanocyte proliferation, cell cycle process, cell cycle, stem cell division, and cell cycle G1-S transition (Figure 4F). mMCPcounter analysis of the tumor RNAseq data predicted an increase in CD8+ T cells (Figure 5A) and monocytes (Figure S6A), and a decrease in B-derived cells and cells of the lymphatics ($p<0.01$) in tumors from the SX-682-treated *Braf/Pten* mice (Figure S6A).

FACS analysis of SX-682 treated *Braf/Pten* tumors revealed a trend toward increased CD8+ T cells ($p=0.17$), no change in CD11b+ cells, and a significant decrease in

CD11b+Ly6G+ cells ($p<0.001$) (Figures 5B, C). Additional FACS analysis of tumor CD45+ cells showed a decrease in CD4+CD3+ cells ($p<0.05$) in tumors from the SX-682 chow-fed mice (Figure S6C). In peripheral blood, there was a significant decrease in CD44+ CD4+ T cells and CD62L+ CD4+ T cells and a trend toward increased CD69+ CD8+ T cells from mice fed SX-682 chow ($p=0.059$; Figure S5B). In addition, a cytokine array of tumor lysates (n=4 for each genotype) revealed a marked reduction in VEGF, indicating a reduction in tumor angiogenesis, and an increase in TNFα, indicating a more inflammatory tumor microenvironment (Figure 5D). Moreover, RNAseq analysis of *Braf/Pten* tumors revealed that SX-682 induces expression of CXCL9, CXCL10, and PD-L1 (Figure 5E). Altogether, these data indicate that SX-682 alters the TME to stimulate anti-tumor immunity and reduce tumor growth.

SX-682 Treatment of Melan-A, B16F0, and B16F10 Cells Reveals Tumor Cell-Specific Gene Modulation

Our murine experiments involved bulk RNA sequencing of tumors that contain tumor cells in addition to stromal and immune cells. In order to identify the specific effect of SX-682 treatment on tumors without the contribution of other cell types, we investigated the effect of SX-682 on non-tumorigenic Melan-A cells, tumorigenic B16F0 cells, and metastatic B16F10 cells *in vitro*. First, we evaluated CXCR2 expression and found that B16F0 and B16F10 cells express significantly more CXCR2 than Melan-A cells, as evaluated by mRNA levels and surface protein labeling (Figure 6A, B). We then analyzed the effect of SX-682 (5 μM) on the growth of these cells and observed that SX-682 treatment resulted in a small but significant inhibition of growth in B16F0 and B16F10 cells *in vitro* based on the percentage of cells staining positively for KI-67

(Figure 6C) and cell number (Figure S7A). In addition, SX-682 treatment of B16F0 and B16F10 cells *in vitro* also reduced production of both CXCL1 (KC) and vascular endothelial growth factor (VEGF) as evaluated by cytokine array (Figure 6D), again indicating the potential for SX-682 to impact the TME.

To identify tumor cell-specific transcriptional changes following SX-682 treatment, we performed RNA sequencing on each of the three cell lines. Of the total differentially expressed genes, expression of 4024 genes was altered in all three lines. An additional 860 genes were differentially expressed in both tumorigenic B16F0 and B16F10 lines in response to SX-682 (Figure S3C and S7B). Commonly upregulated genes include those involved in apoptosis and cell stress response and suppression of gluconeogenesis. In contrast, commonly down-regulated genes include those involved in methylation, RNA splicing, and cell cycle processes (Figure S3C and S7B). Reverse phosphoprotein analysis (RPPA) identified SX-682-induced decreases in phosphoproteins involved in growth (AKT, BRAF, pS445-BRAF, Cdc2-pY15, Cdc6, GSK-3B, mTOR, mTOR pS2448, MMP14, PAX8, and S6), as well as SX-682-induced increases in immunomodulatory proteins (STING, PD-1, PDL1, TRIM25, and Annexin I); proteins involved in the regulation of apoptosis (PUMA, Blc2, Bcl2A1, BclxL, Smac); tumor suppressors (TSC2, WTAP); and cell cycle regulators (Cdc25, CDC42, PLK1, EGFR, PRAS40_pT246). Of interest, β-catenin is increased following SX-682 treatment. This is counter-intuitive for SX-682 inhibition of tumor growth, as the Wnt/β-catenin pathway often drives melanoma tumor growth and metastasis. However, we observed that the phosphorylated forms of β-catenin (pT41 and pS45) that enable its ubiquitin-mediated degradation are also increased. This indicates that β-catenin is being marked

for degradation, thus diminishing the potential for enhanced tumor growth. There were also increases in proteins involved in motility: myosin-Iia, PAK, CDC-42, myosin Iia_pS1943, and HMHA1 (Figure S7C, D). Finally, there were only subtle changes in cytokine expression in response to SX-682 treatment *in vitro,* and these were inconsistent across the three cell lines (Figure S7E). Altogether, these results suggest that multiple compounding signals are induced in cells treated with SX-682, including a decrease in growth signaling, modulation of apoptosis, enhanced anti-tumor immunity, and altered cell cycle processes.

TFCP2L1 distinguishes the WT from the CXCR2 Perturbed Phenotype

To better understand the complex transcriptional reprogramming that occurs when CXCR2 activity is diminished via knockout or with SX-682 treatment, we compared differentially expressed genes in *Braf/Pten/Cxcr2*$^{-/-}$ tumors, SX-682-treated tumors, and SX-682-treated tumorigenic B16F0 and B16F10 cell lines compared to controls. We noted that based upon our search for genes with a minimum of a log2 fold change >2 and a p-value <0.05, only one gene stood out as significantly upregulated across all four models compared to the respective controls: Transcription factor CP2 like-1(*Tfcp2l1)* (Figure 7A,B). To verify the RNA sequencing results, we performed RT-PCR analysis of RNA samples from MelanA, B16F0, and B16F10 cells to determine *Tfcp2l1* expression. With this assay, we show that SX-682-treatment elevates *Tfcp2l1* expression in the tumorigenic cell lines (Figure S9).

TFCP2L1 is a transcription factor that contributes to the maintenance of stemness in pluripotent stem cells and can also exhibit tumor suppressive activity (Kotarba et al.,

2018; Liu et al., 2017; Ouyang Z, 2009; Sun et al., 2018; Zhang et al., 2021). The Krupple-like Factor (KLF) family of transcription factors works with and can be induced by TFCP2L1 to modulate induction and maintenance of naïve pluripotency in mouse primordial germ cells (Qiu et al., 2015; Takashima et al., 2014; Wang et al., 2019). When *Tfcp2l1* is knocked out in mouse embryonic stem cells, there is suppression of expression of other pluripotency genes, including *Nanog, Oct4, Sox2,* and *Esrrb* (Liu et al., 2017), indicating a positive association between *Tfcp2l1* and these genes. When we analyzed our RNAseq data, we observed increased expression of the stemness markers *Tfcp2l1*, *Klf4, and Notch1* in the *Braf/Pten/Cxcr2*$^{-/-}$ tumors. However, the stemness marker *Esrrb* and the neural crest markers *Sox10* and *Foxd3* were significantly decreased in this model. SX-682-treated *Braf/Pten* tumors exhibited increased stemness markers *Tfcp2l1* and *Sox2* with decreased *Notch1 and Sox10* expression (Figures 7C, S8A-L). RT-PCR analysis of RNA isolated from B16F0 and B16F10 cells revealed that SX-682 treatment induced the expression of stemness markers *Tfcp2l1, Nanog,* and *Notch1* and reduced the expression of stemness (*Hmga2, Esrrb, Sox2*), neural crest (*Foxd3, Sox10*), and melanoblast (*Mitf*) markers. SX-682-treatment also enhanced the expression of *Klf4* in B16F10 and MelanA cells (Figure S9).

To support the relevance of Tcfp2l1, we performed an orthogonal approach based on weighted gene co-expression network analysis (WGCNA). WGCNA was applied to the RNA-seq data from these tumors to generate groups of highly correlated genes, or gene modules, that functionally distinguish the *Braf/Pten/Cxcr2*$^{-/-}$ and *Braf/Pten/Cxcr2*^{WT} tumors (Figure S10). Using an ANOVA test between sample conditions, we found six

distinct modules that significantly distinguish *Cxcr2*^{WT} and *Cxcr2*$^{-/-}$ tumors (FDR-adjusted p-value < 0.05; Blue, brown, green, and yellow modules upregulated in *Cxcr2*^{WT} tumors, and turquoise and red modules upregulated in *Cxcr2*$^{-/-}$ tumors, Figure S10). This suggests that there is a clear separation of transcriptional programs between *Cxcr2*^{WT} and *Cxcr2*$^{-/-}$ tumors.

Gene ontology (GO) analysis showed each module is enriched in distinct functions: the *Cxcr2*^{WT}-upregulated modules are enriched in GO terms such as protein localization to mitochondrion (blue, Bonferroni-adjusted p = 0.0002), aerobic respiration and oxidative phosphorylation (green, adjusted p = 1.64×10^{-23} and 1.72×10^{-23}, respectively), and signaling (yellow, adjusted p = 1.65×10^{-12}), while the *Cxcr2*$^{-/-}$-upregulated modules are enriched for GPCR signaling (red, adjusted p = 0.0386) and skin development (turquoise, adjusted p = 2.89×10^{-21}). These changes in gene expression may result as an adaptation to the loss of CXCR2 function. Interestingly, the WGCNA module membership score (kME) indicated that Tfcp2l1 is central to the turquoise module (kME = 0.854) and significantly upregulated in the *Cxcr2*$^{-/-}$ samples (FDR-adjusted p=0.0000286).

Finally, to define the activity of TFCP2L1 following CXCR2 perturbation, we performed chromatin immunoprecipitation and sequencing analysis (CHIPseq) on B16F0 tumorigenic melanoma cells following treatment with vehicle or SX-682. In identifying promoters bound by TFCP2L1 in each condition in addition to RNAseq data, we can delineate SX-682-induced gene set enrichment. Interestingly, enrichment analysis of TFCP2L1-bound genes revealed that SX-682 treatment increased expression of genes associated with T cell differentiation and genes involved in the negative regulation of

cell adhesion (Figure S11A). SX-682 treatment also enriched TFCP2L1 binding to and repression of genes involved in the RAF/MAPK and β-catenin independent Wnt signaling pathways (Figure S11B). When data from RNAseq, RPPA, and ChIPseq analysis were examined using Metascape, key regulatory pathways emerged as commonly associated with CXCR2 loss of function (Figure S11C, D). These data suggest that the SX-682-mediated increase in TFCP2L1 alters gene expression to decrease tumor cohesion, promote T cell differentiation as seen in earlier FACS analysis, diminish MAPK signaling consistent with loss of autocrine CXCR2 stimulation, and modulate Wnt signaling, which is known to contribute to a cancer stem cell-like phenotype.

Does CXCL1 activation of normal melanocytes suppress the TFCP2L1 transcriptional program?

To gain insight into how CXCL1 activation of CXCR2 regulates the expression of stemness and differentiation markers, RNAseq analysis was performed on normal human epidermal melanocyte (NHEM) cultures treated with CXCL1 or with CXCL1 and SX-682 (Figure S12). CXCL1 supplementation was necessary in this model to recreate the enhanced baseline CXCR2 activation of tumorigenic cells. We found that CXCL1 treatment alone induced expression of MITF, BMP6, WNT5A, and SOX10, and the addition of SX-682 reversed this effect while elevating TFCP2L1, KLF4, FOXD3, FOXD1, and CCL20 expression (Figure S12C). In addition to the effects on stemness and differentiation markers, we also found that a number of chemokines and interleukins (Table S1) and TNF-related cytokines and interferons (Table S2) were altered when NHEMs were treated with CXCL1 and SX-682. Taken together, these results suggest that CXCR2 inhibition or

loss of expression in developing melanoma affects the expression of genes associated with melanocyte stemness, differentiation, and cytokine production.

Discussion

The CXCR1 and CXCR2 receptors are G protein-coupled receptors that generate downstream signals including PI3K and AKT, often implicated in growth (Ha et al., 2017 (Sai et al., 2008). (Liu et al., 2019b; Matsushima et al., 2022). The role of CXCR2 in cell motility has been well characterized, but the signals generated through this receptor leading to activation of AKT and ERK also modulate cell proliferation and growth (Li, 2012; Park et al., 2021; Raman et al., 2007; Richmond et al., 2004).

CXCR1 has been reported to be important for the renewal of a population of stem cell-like cells in human breast cancer (Charafe-Jauffret et al., 2009; Ginestier et al., 2010; Schott et al., 2017). In mice, CXCR2 controls functions normally regulated by CXCR1 in humans. Since CXCR2 is thought to be responsible for most of the functional responses to chemokines CXC1-3,5-8, it is plausible that CXCR2 may modulate stemness in breast epithelial cells in the mouse. Here, we examined the role of CXCR2 in melanocyte tumorigenesis and observed that loss of CXCR2 in tyrosinase-expressing melanocytes suppressed melanoma tumor growth and incidence in the *Braf/Pten* murine melanoma model and reduced tumor growth in the *NRas/Ink4a* murine melanoma model.

We observed that the tumors generated in *Braf/Pten* mice with loss of expression of CXCR2 in tyrosinase-positive cells exhibited significant changes in gene expression. A trend toward a reduced expression of genes involved in cell proliferation and increased

expression of genes involved in tumor suppression was observed. We also observed that along with the loss of CXCR2 expression in tumor cells, there was a change in the tumor immune microenvironment, with increased CD8+ T cells and reduced macrophages and MDSC-like cells. Moreover, we observed changes in the phospho-proteomic profile that also reflected inhibition of pathways involved in cell growth in *Braf/Pten* tumors from mice with CXCR2 deletion. When CXCR1/CXCR2 were antagonized by feeding *Braf/Pten* mice chow containing SX-682, there was a similar trend in gene expression profile. Tumors from SX-682-treated mice had a reduction in expression of genes involved in growth and increased expression of tumor suppressors. However, the specific genes modulated were somewhat different in the two models. SX-682 treatment also resulted in an influx of activated CD8+ T cells and the establishment of an anti-tumor immune microenvironment.

To evaluate the melanoma tumor cell-specific effects of CXCR2 inhibition (i.e. independent of effects of immune and stromal cells), we treated B16F0 and B16F10 cell lines with SX-682 *in vitro*. RNAseq analysis revealed that SX-682 treatment results in gene expression consistent with growth-suppression and an anti-tumor immune microenvironment compared to the response of non-tumorigenic Melan-A cells. When we looked for genes commonly induced in *Cxcr2*$^{-/-}$ tumors and SX-682 treated tumors and tumor cells, one common gene emerged, *Tfcp2l1*. *Tfcp2l1* is a crucial transcription factor expressed by embryonic stem cells that induces the expression of genes associated with stemness, including *Nanog, Oct4, Sox2, Esrrb, GATA3,* and *Myc* (Kotarba et al., 2018). We observed a $\log_2$ fold change in *Tfcp2L1* expression greater than 2 across all conditions with CXCR2 perturbation, as well as trends toward

increases in *Nanog* (Sun et al., 2018; Ye et al., 2013), *Klf4* (a pluripotency marker that contributes to ESC maintenance) (Wang et al., 2019), *and Hmga2*, and a significant increase in *Stat3* and *Myc*. However, another marker associated with pluripotency, *Esrrb* (Wang et al., 2019), was decreased with loss of *Cxcr2*. In addition, *Mitf,* a transcription factor associated with the differentiation of melanoblasts, and *Sox10* (a marker of neural crest cells) were both decreased following loss of *Cxcr2* expression or treatment with SX-682. In murine and human melanoma, *Tfcp2,* which is linked to *Tfcp2l1* and *Esrrb*, has been reported to inhibit melanoma tumor growth (Goto et al., 2016; Kotarba et al., 2018). Together, our data indicate that some, but not all, of the stemness markers are increased in association with loss of CXCR2 expression. Moreover, while several markers of differentiation decreased, tyrosinase (*Tyr*) did not decrease.

Much of our understanding of melanocyte lineage came from *in vitro* studies that involved the differentiation of human pluripotent stem cells along a neural crest lineage, then on to form melanocytes (Larribere & Utikal, 2019) (for review). This differentiation process been extensively studied (Larribere & Utikal, 2014; Mica et al., 2013; Zabierowski & Herlyn, 2010). WNTs and BMP4 are involved in the early transition of Oct4+ and Nanog+ pluripotential cells into neural crest cells that express SOX10. If these neural crest cells are exposed to endothelins and BMP4, they transition into melanoblasts that express MITF and cKIT. Under the continued influence of WNTs, BMP4, and induction of intracellular cAMP, melanoblast undergo terminal differentiation into melanocytes that express tyrosinase and OCA2 (Larribere & Utikal, 2014). Interestingly, although our melanoma tumors were driven by tyrosinase induced

alterations in *Braf/Pten/Cxcr2*$^{-/-}$ in melanocytes, we noted a decrease in neural crest markers *Sox10, Foxd3,* and the stemness marker *Esrrb.* At the same time there was an increase in *TFCP2L1, Klf4, Notch1, and HMGA2* when CXCR2 was inhibited or deleted. Moreover, *in vitro* experiments with NHEM showed that CXCL1 stimulation enhanced expression of differentiation markers, while SX-682 prevents this shift and moves the cells toward a somewhat less differentiated state.

Our finding that loss or inhibition of CXCR2 activity in melanocytic cells results in changes in markers associated with stemness, neural crest cells, and melanoblasts in association with a reduction of tumor formation and growth is somewhat paradoxical. However, melanoma tumors are quite heterogeneous, with stem-like cell populations and more differentiated cells expressing MITF, TYR, and MELANA. Of note, nests of stem-like melanoma cells have been identified in metastatic lesions in the head and neck and shown to express *Nanog, Oct4, Sox2, KLF4,* and *cMyc* (Yoganandarajah et al., 2020). Moreover, melanocytes and melanoma cells have been dedifferentiated to iPSCs by transfecting in *Oct4, c-Myc,* and *Klf4* expression vectors. The resulting iPSCs express *Nanog* and *Oct4* and can be differentiated into fibroblast-like cells (Utikal et al., 2009). Our data suggest that loss of CXCR2 signaling may reduce sub-populations of melanoma cells expressing the neural crest marker *Sox10* and stem cell marker *Esrrb* but increases populations with the stemness markers *Klf4* and *Tfcp2l1* and pluripotency genes *Nanog* and *Hmga1*. Single-cell transcriptomics of primary melanoma tumor lesions identified six functionally enriched states of tumor cells: melanocytic, neural crest-like, antigen-presenting, RNA processing, stem-like, and stress-like (Karras et al., 2022). Our data suggest that with the loss of CXCR2 activity during melanoma

induction, these populations are redistributed. Moreover, with this redistribution, tumor growth is reduced.

Altogether, our data demonstrate that targeted deletion of CXCR2 in melanocytes or treatment with CXCR2 inhibitor SX-682 prior to and continuing after induction of *Braf/Pten* or *NRas/Ink4a* reduced tumor burden and expression of genes involved in growth, increased the expression of genes involved in tumor suppression, and increased a population of cells that express stemness markers. Of notable interest, in addition to these changes in gene expression, the tumor immune microenvironment became more tumor suppressive. These data indicate that CXCR2 is involved in many aspects of melanoma tumor growth, including alterations in intracellular signaling, gene expression, and immune cell recruitment. Our data support combining CXCR2 antagonists with immunotherapy for melanoma patients. Consistent with this concept, we have shown that the antagonism of CXCR2 enhances the response of melanoma cells to anti-PD1 (Yang et al., 2021). Moreover, CXCR1/CXCR2 antagonists combined with anti-PD-1 are currently in clinical trials for the treatment of melanoma (NCT03161431). Moving forward, it will be essential to identify the subset of patients most likely to respond to this combination therapy and to develop protocols for maximal response.

Acknowledgments: We thank Dorothea Bennett for the MelanA cell line (University of Texas) and Christine Burd (The Ohio State University School of Medicine) for the *Tyr-CRE-ERT2-NRas^{Q61}R/p16Ink4a$^{-/-}$* mice. We appreciate Tracy Handel (University of California, San Diego) for her helpful comments during the preparation of this manuscript. We are thankful for grant support from NCI R01CA116022 (AR). VA SRCS

Award IK6BX005225 (AR), VA Merit Award 101BX002301 (AR), Lloyd Foundation for Melanoma Research (CY), NCI T32 CA110025-11 (KB), NCI U54 CA217450 (VQ), NCI T32 CA009582 (SG), and NCI T32 CA009592 (AO). Flow Cytometry experiments were performed in the VUMC Flow Cytometry Shared Resource that is supported by the Vanderbilt Ingram Cancer Center (P30 CA68485) and the Vanderbilt Digestive Disease Research Center (DK058404). The Translational Pathology Shared Resource is supported by NCI/NIH Cancer Center Support Grant P30CA068485. Sequencing support was provided by the VUMC VANTAGE Core Facility, also supported by P30 CA68485.

Author Contributions:

J Yang performed the animal experiments, K Bergdorf analyzed the RNAseq data, C Yan analyzed human datasets from multiple sources, e.g., GEO, TCGA, TIDE, Riaz et al., 2017, and Chen et al., 2016, S-C Chen and D Ayers performed the biostatistical analysis, Q Liu, X Liu extracted the raw RNAseq data and provided analysis, W Luo helped with the ChIP-seq experiments, M Boothby provided immunology expertise, S M Groves, AN Oleskie, and V Quaranta assisted with the transcription factor analysis, JA Zebala and DY Maeda provided expertise for SX-682 experiments, A Richmond designed the study, oversaw the gathering and interpretation of data, all the authors contributed to the writing of the manuscript.

Declaration of interests: JA Zebala and DY Maeda are affiliated with Syntrix Pharmaceuticals and provided the drug for these studies. The other authors do not have any competing interests to disclose.

Figure legends:

Figure 1. CXCR2 associated with tumorigenesis and poor prognosis. GEO dataset analysis of expression of CXCR1 and CXCR2 in nevi as compared to melanoma lesions (A). GEO dataset analysis of expression of CXCL1, CXCL2, CXCL3, CXCL5 and CXCL8 in nevi and melanoma tissues (B). Overall survival plot of melanoma patients from the TCGA SKCM dataset indicates significantly improved survival (p=0.035) in the lowest quartile of CXCR2 expression (blue, n=107) compared to the highest quartile (red, n=114) (C). Analysis of survival of 25 melanoma patients treated with anti-PD1 in relation to high (red) or low (blue) expression of CXCR2 (p<0.01; Liu et al., 2019a) (D). Re-analysis of the Riaz RNA-seq database shows CXCR2 expression is lower in melanoma patients who responded to anti-PD1 treatment (p<0.05) (E). Statistical analyses: (A), (B), and (E) Welch's t-test; (C), (D) log-rank test.

Figure 2. CXCR2 impacts on melanoma tumor burden. *Tyr-Cre*$^{ER+}$*:: Braf*$^{CA/+}$*::Pten*$^{lox4-5/Lox4-5}$*::mT/mG* C57BL/6 mice were crossed with floxed *Cxcr2* mice to obtain mice with inducible tumors with or without CXCR2 expression Thirty-six days after 4-HT administration, skin tumour volume (A) and count(B), were recorded and mice were photographed (C). Similarly, *Tyr-Cre*$^{ER+}$*::NRas*^{Q61R}*::Ink4a*$^{-/-}$*::mT/mG* mice were crossed with floxed *Cxcr2* mice, and resulting pups were treated with 4-HT on days 1 and 2 prior to UV irradiation on day 3 to initiate tumor formation (n=16/genotype). Tumors were measured (D), counted (E), and mice were photographed (F). RNA was extracted from *Braf*^{V600E}*/Pten*$^{-/-}$*/Cxcr2*$^{-/-}$ and *Braf*^{V600E}*/Pten*$^{-/-}$*/Cxcr2*^{WT} tumors and subjected to RNAseq analysis. A volcano plot showing fold change and significance of differential gene expression in *Cxcr2*$^{-/-}$ tumors compared to *Cxcr2*^{WT} tumors (G). Gene set enrichment

analysis (GSEA) of RNAseq data identifies 8 gene sets enriched in *Cxcr2*$^{-/-}$ tumors. Point size indicates the gene ratio (percent of genes from the gene set contributing to the enrichment score) and point color represents the FDR q-value (H). Statistical analyses: (A), (B), (D), (E) Welch's t-test

Figure 3. The immune infiltrate of *Braf*^{V600E}*/Pten*$^{-/-}$ tumors is altered with loss of *Cxcr2.* mMCPCounter analysis performed on bulk RNAseq data from *Braf*^{V600E}*/Pten*$^{-/-}$ melanoma tumors with or without CXCR2 predicts significantly enhanced infiltration of T cells, CD8+ T cells, monocytes, NK cells, and lymphatic vessels into *CXCR2*$^{-/-}$ tumors *(*A). FACS analysis of CD45+ myeloid cells in *Braf*^{V600E}*/Pten*$^{-/-}$ melanoma reveals decreased MDSC-like cells in *CXCR2*$^{-/-}$ tumors (B). FACS analysis of CD45+ cells in *Braf*^{V600E}*/Pten*$^{-/-}$ melanoma tumors identified changes in activated CD4+CD44+ T cells and CD8+CD69+ T cells (C). Cytokine array for 62 cytokines expressed in TME of *Braf*^{V600E}*/Pten*$^{-/-}$ tumors revealed one major cytokine, CCL20, that is strongly upregulated with loss of CXCR2 (n=4/genotype) based on net density. These data are complemented by increased *Ccl20* mRNA with loss of *Cxcr2* in *Braf*^{V600E}*/Pten*$^{-/-}$ tumors (D). CXCL9, CXCL10, and PD-L1 expression based upon RNAseq analysis from *Braf*^{V600E}*/Pten*$^{-/-}$ tumors expressing or not expressing CXCR2 in melanocytes (E). Statistical analyses: (A), (B), (C), (D), (E) Welch's t-test

Figure 4. SX-682 affects *Braf*^{V600E}*/Pten*$^{-/-}$ and *NRas*^{Q61R}*/Ink4a*$^{-/-}$ tumorigenesis. *Braf*^{V600E}*/Pten*$^{-/-}$ (A, B) and *NRas*^{Q61R}*/Ink4a*$^{-/-}$(C, D) mice were fed chow containing SX-682 or vehicle continuously through tumor formation, and tumors were measured (A,C) and counted (B,D). A volcano plot showing fold change and significance of differential gene expression between tumors from SX-682-fed and control-fed *Braf*^{V600E}*/Pten*$^{-/-}$ mice

(E). Gene set enrichment analysis of SX-682 treated or control *Braf*^{V600E}/*Pten*$^{-/-}$ tumors identifies gene sets enriched in SX-682 treated tumors (positive normalized enrichment score) or enriched in control tumors (negative normalized enrichment score) (F) Statistical analyses: (A), (B), (C), (D) Welch's t-test

Figure 5. SX-682 alters the immune profile of *Braf*^{V600E}/*Pten*$^{-/-}$ melanoma. mMCPCounter analysis of bulk RNAseq data predicts enrichment for CD8+ T cell infiltrate into tumors following treatment with SX-682 ($p<0.05$) (A). FACS analysis confirms significantly increased presence of CD8+ T cells in SX-682 treated *Braf*^{V600E}/*Pten*$^{-/-}$ melanoma (B). FACS analysis of CD45+ myeloid cells indicated a significant decrease in immunosuppressive CD11b+Ly6G+ cells, but no change in total CD11b+ cells (C). A cytokine array was performed on control and SX-682 treated tumors, identifying a notable decrease in VEGF and an increase in TNFα (D). CXCL9, CXCL10, and PD-L1 expression based upon RNAseq analysis from SX-682 or control treated tumors (E). Statistical analyses: (A), (B), (C), (D), (E) Welch's t-test

Figure 6. Tumor cell-specific impacts of SX-682. CXCR2 expression on Melan-A, B16F0, and B16F10 cells based on the NCBI database (A) and flow cytometry (B). Cell lines were treated with 5 µM SX-682 (or DMSO control) for 4 days prior to staining with Pacific Blue-Ki67 for FACS analysis. The percentage of positive staining cells was significantly decreased in the SX-682 treated cells for all cell lines (statistical analysis: two-way ANOVA with Benjamini and Hochberg (BH) correction for multiple tests) (C). Cytokine array of SX-682-treated MelanA, B16F0 and B16F10 cells shows that SX-682 treatment reduced the expression of KC and VEGF in all three cell lines (D).

Figure 7. TFCP2L1 is commonly upregulated across three models of CXCR2 perturbation. In comparing expression data from *Braf*^{V600E}*/Pten*$^{-/-}$*/Cxcr2*$^{-/-}$ tumors. *Braf*^{V600E}*/Pten*$^{-/-}$ tumors treated with SX-682, and B16F0 and B16F10 cell lines treated with SX-682, *Tfcp2L1* was consistently upregulated compared to appropriate controls (A,B). Log_2 fold change for *Tfcp2l1* and related genes across experimental groups based upon RNAseq analysis (C). TFCP2L1 Transcription network from the Gene Analytics database (D). Identification of transcription factors central to Weighted Correlation Network Analysis (WGCNA) co-expressed gene modules (by kME) and significantly differentially expressed between *Braf*^{V600E}*/Pten*$^{-/-}$*/Cxcr2*$^{-/-}$ and *Braf*^{V600E}*/Pten*$^{-/-}$*/Cxcr2*^{WT} tumors. TFs are colored by gene module and show varying levels of centrality to each module and importance in distinguishing WT and KO tumors (E). Statistical analyses: (B) Welch's t-test

Supplemental Figure Legends:

Figure S1. Breakdown of CXCR2 (A) and CXCL1 (B) expression in nevi and melanoma from TCGA, separated based on BRAF and NRAS mutation status. Data were analyzed with a two-way ANOVA and no significant differences were found.

Figure S2. Diagram showing strategy for development of *Tyr-Cre*^{ER}*::Braf*^{V600E}*::Pten*$^{-/-}$*::mT/mG*$^{fl/fl}$*::Cxcr2*$^{fl/fl}$ and *Tyr-Cre*$^{ER+}$*::NRas*^{Q61R}*::Ink4a*$^{-/-}$*::mT/mG*$^{fl/fl}$*::Cxcr2*$^{fl/fl}$ mice (A, B, figures created using Biorender). Image of GFP-expressing *Braf*^{V600E}*/Pten*$^{-/-}$ tumors *in vivo* and via histology (C, D).

Figure S3. Heat maps of the most differentially expressed genes in tumors from the *Braf*^{V600E}*/Pten*$^{-/-}$ mice with or without loss of CXCR2 in tumor cells (A), with control or

SX-682 treatment (B), and in MelanA, B16F0, and B16F10 cells treated with DMSO or SX-682 (C). Tumor suppressive genes are listed in red, genes involved in growth are in green, immune related genes are in blue, differentiation/stemness genes are in purple, and motility and cell adhesion genes are in brown.

Figure S4. Heat map showing genes involved in growth that are suppressed (A) and genes involved in growth suppression that are induced (B) in *Braf*^{V600E}/*Pten*$^{-/-}$/*Cxcr2*$^{-/-}$ melanoma tumors. Red arrows indicate genes involved in growth/oncogenes (A) and inhibition of growth/tumor suppression (B).

Figure S5. Additional data from analysis of immune cells and cytokines expressed by *Braf*^{V600E}/*Pten*$^{-/-}$/*Cxcr2*$^{-/-}$ and *Braf*^{V600E}/*Pten*$^{-/-}$/*Cxcr2*^{WT} tumors. mMCPCounter predicted infiltrate of B-derived cells, memory B cells, neutrophils, endothelial cells, mast cells, basophils, eosinophils, and blood vessels (A). FACS analysis of peripheral blood CD45+ cells from *Braf*^{V600E}/*Pten*$^{-/-}$/*Cxcr2*$^{-/-}$ and *Braf*^{V600E}/*Pten*$^{-/-}$/*Cxcr2*^{WT} mice (B). Results of cytokine array of tumor lysates from *Braf*^{V600E}/*Pten*$^{-/-}$/*Cxcr2*$^{-/-}$ and *Braf*^{V600E}/*Pten*$^{-/-}$/*Cxcr2*^{WT} melanoma tumors, expressed as fold change in *Cxcr2*$^{-/-}$ compared to *Cxcr2*^{WT}(CCL20 removed and shown in Figure 3D to allow proper visualization) (C). FACS analysis of CD45+ cells from *Braf*^{V600E}/*Pten*$^{-/-}$/*Cxcr2*$^{-/-}$ and *Braf*^{V600E}/*Pten*$^{-/-}$/*Cxcr2*^{WT} tumors (D). Statistical analyses: (A), (C), (D) Welch's t-test

Figure S6. Additional data from analysis of immune cells from SX-682-treated *Braf*^{V600E}/*Pten*$^{-/-}$/*Cxcr2*^{WT} tumors. mMCPCounter predictions for T cells, B-derived cells, memory B cells, NK cells, endothelial, monocytes, macrophages, fibroblasts, lymphatics, mast, basophils, eosinophils, and blood vessels (A). FACS analysis of peripheral blood CD45+ cells from tumor-bearing mice fed SX-682 or control chow (B).

FACS analysis of CD45+ cells in SX-682 treated or control tumors (C). Statistical analyses: (A), (B), (C) Welch's t-test

Figure S7. Effects of SX-682 on MelanA, B16F0, and B16F10 cell lines. MelanA, B16F0, and B16F10 cells were treated with SX-682 (5μM) or DMSO, and cell number was evaluated at days 1-4 post treatment. Data were analyzed on a natural log scale and compared using two-way ANOVA with BH correction for multiple tests. (A). Cell lines were treated for 24 hours with SX-682 or DMSO prior to RNA isolation and sequencing. A heat map shows that genes were commonly suppressed or induced in all three cell lines (B). Reverse-phase phosphoproteome analysis (RPPA) was also performed on cells treated for 24 hours with SX-682 or DMSO. Volcano plot showing phosphoproteins commonly altered by SX-682 treatment in MelanA, B16F0, and B16F10 cells (C). A heat map showing differential expression of commonly suppressed or induced phosphoproteins in response to treatment with 5μM SX-682 for 24 hours (D). Cytokine array of cell lysates from MelanA, B16F0, and B16F10 cells treated with SX-682 (5μM) for 24 hours as compared to those treated with DMSO (E).

Figure S8. Expression of *Tfcp2l1*-related genes and tumor markers based on RNAseq analysis in $Braf^{V600E}/Pten^{-/-}/Cxcr2^{-/-}$ tumors, $Braf^{V600E}/Pten^{-/-}$ tumors treated with SX-682, and cell lines (MelanA, B16F0, and B16F10) treated with SX-682 compared to appropriate controls. Statistical analysis: Welch's t-test

Figure S9. Expression of Tfcp2l1-related genes based upon RT-PCR analysis. MelanA, B16F0, and B16F10 cells were treated with SX-682 (5μM) for 24 hours prior to RNA extraction, quantification, and RT-PCR using primers specific for *Tfcp2L1, Foxd3, Sox2,*

Sox10, Notch1, Hmga2, Mitf, Klf4, Myc, Nanog, Esrrb and Tyr. Data are plotted as fold-change compared to DMSO treated cultures. Statistical analysis: Welch's t-test

Figure S10. WGCNA orders genes into a dendrogram by their co-expression profiles across the samples. Gene modules at the bottom of the dendrogram show assignment into distinct clusters of co-expressed genes (A). Module eigengene expression value shown as a heatmap across WT and KO samples (B). Feature selection of modules by ANOVA F-value (FDR-adjusted p-value). 6 of 10 WGCNA gene modules can distinguish between conditions (C). Eigengene expression value across WT and KO samples shown as a bar-plot and significance of transcription factors (ordered by FDR-adjusted p-value) within each module for the six significant gene modules from panel D: blue, turquoise, brown, green, yellow, and red. These TFs are best at distinguishing between KO and WT samples in each module (D).

Figure S11. ChIPseq analysis of changes in gene promoter binding of TFCP2L1 antibody in B16F0 cells in response to SX-682 treatment. B16F0 cells were cultured overnight with either DMSO or SX-682. Cell extracts were incubated with anti-IgG or anti-TFCP2L1, cross-linked with a reversible cross-linker, and prepared and prepared for ChIP-seq analysis. Metascape analysis was used to examine enriched terms across input gene lists of SX-682 minus DMSO, colored by p-values. Top Terms associated with TFCP2L1 bound promoters where gene expression was increased (C) and decreased (D) were identified. Metascape Analysis was used to compare the data sets from RPPA, ChIP, and RNAseq analyses of B16F0 cells treated with SX-682 as compared to vehicle control (C) and (D).

Figure S12. NHEM cells were cultured in melanocyte growth medium containing vehicle or CXCL1 (100ng/ml), or CXCL1 (100ng/ml) with 5 µM SX-682. After 5 days of culture, the cell number was determined and total RNA was extracted for RNAseq analysis. Effects of SX-682 on cell growth in vitro (A). Heatmap for RNAseq on NHEM. 5 days after NHEM was cultured with SX-682 and/or CXCL1, RNA was extracted and subjected to RNAseq analysis(B). Expression values for key genes associated with response to CXCL1 or CXCL1 and SX-682 (C).

Table S1. Comparison of Cytokine, Chemokine, and Interleukin Expression Following CXCL1 or CXCL1+SX-682 Treatment. Key cytokines induced are highlighted in red and reduced are highlighted in green.

Table S2. Comparison of TNF-Related Cytokines and Interferon Expression Following CXCL1 or CXCL1+SX-682 Treatment. Key cytokines induced are highlighted in red and reduced are highlighted in green.

Methods:

RNA-Seq analysis of CXCL1, 2, 3, 5, and 8 from utilized patient nevi and melanoma samples available at NCBI Gene Expression Omnibus (GEO) under accession number GSE112509, including human nevi (n=23) and melanoma (n=57) samples. Bulk RNA-Seq analysis was performed as described previously (Yan & Richmond, 2021). Differential mRNA gene expression was determined and normalized with the DESeq2 tool (Love et al., 2014) (Figure 1A, 1B). To analyze patient overall survival in reference to high or low CXCR2 expression, the Cancer Genome Atlas (TCGA) skin cutaneous melanoma (SKCM) dataset was analyzed using the Gene Expression Profiling

Interactive Analysis (GEPIA) program. To generate the overall survival plot, the upper and lower quartiles of *CXCR2* expression were used to stratify the groups (Figure 1C). For analysis of the CXCR2 expression level predictive value in therapeutic response to immune checkpoint blockade in melanoma patients a Kaplan-Meier plot of overall survival was constructed by Tumor Immune Dysfunction and Exclusion (TIDE, http://tide.dfci.harvard.edu/) platform in patients with melanoma (Fu J, et al, 2020) stratified by CXCR2 z-scores of RNA-Seq normalized count. The P value was calculated by testing the association between prediction scores and overall survival with the two-sided Wald test in a Cox-PH regression [Jiang P, et al., 2018) (Figure 1D, E).

Cell lines and establishment of Inducible melanoma mouse models. `

B16F0 (Catalog number: CRL-6322) and B16F10 (Catalog number: CCL-6475, ATCC) are spontaneous murine melanoma cell lines derived from a C57BL/6J mouse**.**. They are tumorigenic and metastatic clones, respectively. Melan-A is a nontumorigenic murine cell line that is syngeneic with B16 melanoma lines (Bennett et al., 1987). Normal human epidermal melanocytes (NHEMs) were purchased from Lonza (#CC-2504) and cultured in melanocyte growth medium including the MM-4 Bullet kit (Lonza, #CC-2349). To examine the regulation of CXCL1/CXCR2 signaling in NHEM, these cells were stimulated with either vehicle, CXCL1 (100ng/ml) or CXCL1+SX692 (5µM) for 24 hours. MelanA and B16 cells were cultured in DMEM/F12 medium (Gibco, #11330-032) containing 10% FBS (Sigma, PAA, A11-201). After 5 days of culture, the culture medium was removed, cells were trypsinized, aspirated, and collected by centrifugation, resuspended in serum containing medium, and the cell number was determined by Countess II (Invitrogen, C10228). Simultaneously, aliquots of cells were permeabilized

and stained with Pacific Blue-KI67 and analyzed by flow cytometry. Experiments were conducted in duplicate and repeated once. Data were statistically analyzed with the Student's t-test. In other experiments, NHEMs were treated with CXCL1 (100ng/ml) or vehicle, or with SX-682 and CXCL1 for 24 hours before RNA was extracted and processed for RNAseq analysis.

We utilized the inducible *Braf*^{V600E}*/PTEN*$^{-/-}$ melanoma model in C57BL/6 mice (Dankort et al., 2009), where the underlying genetic background includes *Tyr-Cre*$^{ER+}$*:: Braf*^{CA}*::Pten*$^{lox4\text{-}5/Lox4\text{-}5}$. CXCR2$^{f/f}$ mice *(C57BL/6-CXCR2*$^{tm1RMra/J}$*)* were obtained from Jackson Laboratories (#024638) and \ bred to mT/mG mice (#007907, Jackson Laboratories), which harbor a two-colour fluorescent Cre-reporter allele to enable GFP-based tumor imaging (Figure S2A,C) (Muzumdar et al., 2007). In crossing the *Braf*^{V600E}*/PTEN*$^{-/-}$ mice with CXCR2$^{fl/fl}$ mT/mG mice, Tyr-*Cre*$^{ER+}$*::Braf*^{CA}*::Pten*$^{lox4\text{-}5/Lox4\text{-}5}$*::mT/mG::Cxcr2*$^{fl/fl}$ mice and *Cre*$^{ER+}$*:: Braf*^{CA}*::Pten*$^{lox4\text{-}5/Lox4\text{-}5}$*::mT/mG::Cxcr2*^{WT} mice were generated.

Upon administration of 4-HT (#6278, Sigma), Cre-recombinase expression is induced in tyrosinase (*Tyr*) expressing cells, leading to expression of the *Braf*^{V600E} transgene and deletion of exons 4 and 5 of *Pten* specifically in tyrosinase expressing melanocytes (Figure S2B)(Dankort et al., 2009). Palpable tumors arise within one month post 4-HT induction (Figure S2B, C). Tyr-Cre targeting of melanocytes in hair follicles was verified by H&E staining and GFP expression (Figure S2D).

To generate our inducible *NRas* mutant/*Ink4a* deletion/CXCR2 knockout melanoma mouse model, we utilized the *TpN*^{61R} model from Burd et al., which recapitulates the genetics of *NRas*^{Q61R}*/INK4a*$^{-/-}$ mutant human melanoma and demonstrates sensitivity to

UV-induced melanoma (Burd et al., 2014). In this model, expression of mutant *NRas* and loss of *Ink4a* are under the control of the Tyr-promoter enhancer *(Tyr-Cre^{ER}::NRas^{Q61R}::Ink4a$^{-/-}$).* These mice were crossed with C57BL/6 *Cxcr2$^{f/f}$* mice. Heterozygous offspring were crossed to generate *Tyr-Cre^{ER}::NRas^{Q61R}::Ink4a$^{fl/fl}$::Cxcr$^{fl/fl}$ and Tyr-Cre^{ER}::NRas^{Q61R}::Ink4a$^{fl/fl}$::Cxcr2^{WT}* littermates*.* Newborn mice (1-2 days of age) receive one topical administration of 2µl of 20mM 4HT on the back followed by exposure to 4.5K J/m2 UVB radiation (312NM 2X8 Watt tubes& Filter, Cat. # EB-280C) on day 3. Tumor development was followed for 5 months.

To evaluate the effect of the dual CXCR1/CXCR2 inhibitor SX-682 on tumor growth, *Braf^{V600E}/PTEN$^{-/-}$* mice were fed with either SX-682 chow (0.756 g/kg of SX-682, Syntrix Pharmaceuticals, Inc) or control chow for two weeks prior to tumor induction via topical administration of 2µl of 5mM 4-HT onto the dorsal skin of 4-week-old mice for three successive days. The mice continued to be fed on the SX-682 chow or control chow until tumors grew to a volume of 1.5 cm^3 or required euthanasia due to ulceration or another humane endpoint. *NRas^{Q61R}/Ink4a$^{-/-}$* mice pups exposed to 4-HT and UV irradiation were weaned at 21 days and placed on SX-682 or control chow. Tumor volume was measured by microcalipers and tumor number for each mouse was counted after a period of 5 months.

Flow cytometry analysis and antibodies

For flow cytometry analyses, tissues were minced on a programmable dissociator and digested with an enzyme solution of collagenase 1 (1,500 CDU, CAT#234153, Calbiochem), dispase II (1 mg/mL, CAT#13689500, Roche), and DNase 1 (0.1 mg/mL,

CAT#260913, Calbiochem). The details of staining and flow cytometry analyses protocols can be found in our previous published methodology (Yang et al., 2021). Mouse tumors were cut into 1- to 2-mm slices and digested in buffer containing 2 mg/mL collagenase and 0.1 mg/mL DNase I. Digested tumors were passed through a 70-mm strainer to obtain a single-cell suspension. Mouse spleens were pressed through 40 mm strainer using syringe plunger to obtain a single-cell suspension. Red blood cells present in whole blood or cell preparations were removed using ACK Lysing Buffer (CAT#RGF-3015, KD Medical) prior to the staining. Cells were incubated with Ghost Dye TM Violet 510 (Tonbo Biosciences), an amine reactive viability dye used to discriminate live/dead cells and washed with FACS buffer (PBS containing 2% v/v FBS). After blocking Fc receptors with anti-mouse CD16/CD32 mAb in FACS buffer for 15 minutes, cells were incubated with mAbs (BioLegend) to mouse CD45-APC/Cy7, CD3-Alexa Fluor 594, CD4-FITC, CD8a-PE, CD44-APC, CD62L-Alexa Fluor 700, CD25-Percp/Cy5.5, CD69-pacific blue; CD45-Alexa Fluor 488, CD11b-PE, F4/80-Brilliant violet 421, Ly6C-APC, Ly6G-PE/Cy7, MHC II-Alexa Fluor 700, CD206-Percep/Cy5.5, etc. 1 hour on ice. Cells were washed twice in FACS buffer and data acquired with FACSCanto II (Becton Dickenson). For intracellular staining after surface staining, cells were fixing/permeabilizing using Transcription Factor Buffer Set (Cat:562674, BD Pharmingen) per manufacture's protocol. FACS data, comparing leukocytes from $CXCR2^{-/-}$ to $CXCR2^{WT}$ were analyzed using FlowJo software (Version 10.1).

Cytokine Array

Tumor lysate or supernatant of cultured cells were prepared as previously described (Yang et al., 2021). For cultured cell lines, $3x10^5$ cells were plated per well into 6-well plates and incubated overnight. Cells were then treated for 24 hours with 5μM SX-682 (Syntrix) or DMSO prior to supernatant collection. Supernatants were centrifuged to remove cell debris prior to analysis, and both tumor lysates and cell supernatant were subjected to analysis with the Raybio Mouse Cytokine Antibody Array G-Series 3 (Cat# AAM-CYT-G3-8, RayBiotech) per manufacturer's protocol. The glass chip was scanned on the Cy3 channel of a GenoPix 4000B scanner (Genopix 6.1, Molecular Devices, Sunnyvale, CA). For each spot, the net density was determined by subtracting the background. The relative fold difference in cytokine amount was determined in reference to the amount present on the control samples.

RNA extraction and RNAseq analysis

RNA was extracted from tumor tissues or cultured cells using the RNeasy Plus Mini Kit (Cat#74134, Qiagen) per manufacturer's protocol. RNAseq was performed using an Illumina next-generation sequencing platform at the Vanderbilt University Medical Center VANTAGE (Vanderbilt Technologies for Advanced Genomics) Core Facility. Adapters were trimmed by Cutadapt. After trimming, reads were mapped to the mouse genome GRCm38.p6 using STAR and quantified by featureCounts. DESeq2 was used to normalize expression prior to analysis unless otherwise stated. Data were analyzed using GSEA (4.1.0). Gene sets analyzed include:

GOBP_CD4_POSITIVE_ALPHA_ BETA_T_CELL_ACTIVATION, GOBP_LYMPHOCYTE_ACTIVATION, GOBP_ LEUKOCYTE_PROLIFERATION, GOBP_LYMPHOCYTE_ANERGY, GOBP_IMMUNE_ RESPONSE, GOBP_STEM_CELL_DIFFERENTIATION, GOBP_ADAPTIVE_IMMUNE_ RESPONSE,

GOBP_STEM_CELL_DIVISION, GOBP_CD8_POSITIVE_ALPHA_BETA_ T_CELL_ACTIVATION, GOBP_T_CELL_MEDIATED_IMMUNE_RESPONSE_TO_TUMOR_CELL, GOBP_IMMUNE_RESPONSE_TO_TUMOR_CELL, GOBP_ANTIGEN_ PROCESSING_ AND_ PRESENTATION, GOBP_CD8_POSITIVE_ALPHA_BETA_T_ CELL_PROLIFERATION, GOBP_T_CELL_MEDIATED_CYTOTOXICITY, GOBP_ CELL_CYCLE_PROCESS, GOBP_CELL_CYCLE, GOBP_CELL_CYCLE_G1_S_ PHASE_TRANSITION, and GOBP_MELANOCYTE_PROLIFERATION (Human Molecular Signatures Database-MSigDB). For GSEA, 1000 permutations were performed and human orthologs were annotated with Mouse_Gene_Symbol_Remapping_Human_ Orthologs_MSigDB.v2022.1.Hs.chip. Phenotype permutation was used except when the sample size per phenotype was less than 7. In this case, we follow the GSEA recommendation to use gene set permutation.

For expression plots, DESeq2 normalized counts were transformed by adding one to the value (to retain 0s) and then taking the natural log to account for variance. Comparisons were made using a Mann-Whitney test where appropriate.

For murine microenvironment cell population counter (mMCPcounter) analysis, each count file of protein coding genes was normalized to transcripts per million (TPM) as recommended by the program. TPM was calculated by determining rate as the raw counts divided by the gene length, and then dividing each rate by the sum of all rates multiplied by 1e6. Following TPM normalization, data were transformed utilizing log2(TPM normalized expression +1). The mMCPcounter (v1.1.0) package was installed and the function mMCPcounter.estimate was used to determine predicted immune cell infiltrate.

Weighted gene co-expression network analysis (WGCNA)

WGCNA (Langfelder and Horvath 2008) was performed on log-transformed, normalized RNA-seq data of 16382 genes from 15 mouse tumor samples (n = 7 WT mice and n = 8 KO mice) using the R package "WGCNA." A signed network was generated, such that only positively correlated genes were grouped into modules (negative correlations are given a score of 0), as follows. The function pickSoftThreshold was used to determine the exponent of the correlation coefficients matrix which, when used as weights of network connections, best produces a scale-free network. A power value of 20 was chosen. A topological overlap matrix of network adjacencies between genes was then generated with the adjacency and TOMsimilarity functions, using the Pearson correlation function, which gave a distance measure to be used with average-linkage hierarchical clustering. The WGCNA function cutTreeDynamic was used, with minimum module size of 100, deepSplit = 2, and pamRespectsDendro = FALSE, to generate modules of co-expressed genes. Differentially expressed gene modules across WT and KO conditions were determined using an ANOVA statistical test with FDR correction using the python function selectFDR from the Sci-Kit Learn package. Six gene modules could significantly distinguish between the WT and KO tumors (FDR-adjusted p-value < 0.05) (Wooten, 2019).

Identification of Transcription Factor Network Structure

To determine the most important transcription factors (TFs) that both distinguish WT and KO conditions and were central to a gene module, we calculated the module membership value, or kME, for each TF, a measure of correlation of its gene expression

with the module eigengene from WGCNA. TFs were filtered to those with a significant FDR-adjusted p-value for the ANOVA between WT and KO (< 0.05). We then chose the top 40 significant TFs by kME for each of the six significant gene modules to find the most central TFs for each module.

Epigenome mapping by ChIPmentation for TCPF21

ChIPmentation was performed as previously described (Xu et al., 2020; Krausgruber et al., 2020) with some modifications. Cells were treated with 5μM SX-682 or DMSO vehicle for 24 hours, collected by trypsinization, and resuspended in PBS. Next, cells were fixed with fresh formaldehyde at final concentration of 1% for 10 min at room temperature. Glycine was added to final concentration of 0.125 M to quench the reaction. Cells were resuspended at $1x10^7$/ml in sonication buffer (10 mM Tris-HCl pH 8.0, 2 mM EDTA pH 8.0, 1% SDS, with Protease Inhibitor Cocktail (Roche) and PhosSTOP™ Phosphatase Inhibitor Cocktail (Roche) and sonicated for 25-30 sec with Diagenode One sonicator in a 50 ul Bioruptor® One Microfluidic Chip till most DNA fragments were in the range of 200 to 700 bp. After sonication, the lysate was adjusted to RIPA buffer conditions (10 mM Tris-HCl pH 8.0, 1 mM EDTA pH 8.0, 140 mM NaCl, 1% Triton X-100, 0.1% SDS, 0.1% sodium deoxycholate, with Protease Inhibitor Cocktail and PhosSTOP™ Phosphatase Inhibitor Cocktail). For each immunoprecipitation, lysate from $2x10^6$ cells and 6 μg of anti-TFCP2L1 antibody (Boster Bio) were used. 6.0 μg of normal rabbit IgG was used as a control. 40μl Dynabeads ™ Protein A (Invitrogen) were used in each immunoprecipitation. After immunoprecipitation, beads were washed twice with RIPA low-salt buffer, twice with

RIPA high-salt buffer, twice RIPA lithium-chloride buffer, and once with 10 mM Tris-HCl buffer (pH 8.0). Illumina sequencing adapters were added on bead-bound DNA fragments via tagmetation by using Illumina Tagment DNA TDE1 Enzyme and Buffer Kits (Illumina). After tagmentation, bead-bound DNA fragments were extracted by reversing the crosslink and proteinase K digestion. DNA fragments were purified with AMPure XP beads (Beckman Coulter). qPCR was performed first with KAPA HiFi HotStart Ready Mix and a pair of Nextera custom primers to determine the optimum number of PCR cycles for the DNA library preparation for each immunoprecipitation. The final enriched DNA library for each immunoprecipitation was created by PCR with KAPA HiFi HotStart Ready Mix and Nextera custom primers using the optimum number of PCR cycles determined by qPCR. The enriched DNA library was purified with AMPure XP beads, and size-selection was performed by controlling the concentration of ethanol in the AMPure XP beads and DNA mixture. Acquired DNA libraries were sequenced by the Illumina NovaSeq 6000 platform at Vanderbilt Technologies for Advanced Genomics core laboratory. ChIPmentation reads were aligned to the mouse reference genome mm10 using Bowtie2 (Langmead and Salzberg, 2012). Peaks for each sample were called by MACS2 with an FDR cutoff of 0.01 and the corresponding IgG input as the control (Feng, et al., 2012; Feng, et al., 2011; Zhang, et al., 2008). Peaks were annotated using Homer (http://homer.ucsd.edu/homer/) and assigned to their closest genes. Enriched motifs were identified by the Homer command findMotifsGenome with the default region size and the motif length (-size 200 and -len 8, 10, 12). Genes that had TFCP2L1 bound to their 5' promoter in the DMSO and SX-682-treated samples were selected and analyzed further using Metascape software (Zhou Y,

et al., 2019). Comparisons were made among RPPA, RNAseq, and ChIPseq data sets for B16F0 cells using Metascape software to identify commonly enriched pathways.

RT-qPCR

B16F0, B16F10, and MelanA cells were treated with 5µM SX-682 or DMSO for 12 hours prior to collection and RNA extraction with Trizol. cDNA was generated using a Reverse Transcription kit (Catalog number M510A, Promega), and qPCR was performed using a BioRad CFX-qPCR instrument and SsoAdvanced Universal SYBR Green Supermix (Cat: 172-5270, BioRad). Fold changes were calculated using the formula $2^{-(\Delta\Delta Ct)}$, where $\Delta\Delta Ct = \Delta Ct^{(SX\text{-}682)} - \Delta Ct^{(DMSO)}$. The Ct is the cycle at which the threshold line is crossed. Primers for β-actin, sense-ACATGGCATCATCACCAACTG and antisense-AGAATCCAACACGATGCCGG. TFCP2L1, sense-ACACTACAACCAGCACAACTC and antisense-TGGTACTCTGTG TACTGCAGC. Sox10, sense-ACCTATCAGAGGTGGAGCTGAG and antisense-TGC TGTTCCTTCTTGACCTTG. MITF, sense-AGAGCAGCAGTTCTGCAGAGC and antisense-ATGGCTGGTGTCTGACTCACG. Nanog, sense-TCTGCTACTGAGATG CTCTGC and antisense-ACAGTCCGCATCTTCTGCTTC. FoxD3, sense-AGCGATA TGTCCGGCCAGACG and antisense-TGAGACTGGCCGTGATGAGCG. Notch1, sense-TGACTGTACTGAGAGCTCCTG and antisense-AAGTACCATAGCTGTCTTGGC. TLF4, sense-ATGGCTGTCAGCGACGCTCTG and antisense-TGTTACTGCTGCAAGCTG CAC. Slc4A1, sense-ACTGGAGAACATAATAGGACAG and antisense-AAGGTCAGG TAAGATAGATGTG. Esrrb, sense-AGTGCGAGTATATGCTTAATG and antisense-

TGAATTGTCCTCTTGAAGAAG. Sox2, sense-ATGATGGAGACGGAGCTGAAG and antisense-TTGCTGATCTCCGAGTTGTGC. HMGA2, sense-TGCCACAGAAGCGAGGA CGCG and antisense-TCCTAGGTCTGCCTCTTGGCC.

Protein extraction and RPPA analysis

Melan-A, B16F0, and B16F10 cells were seeded at a density of $3x10^5$ per well in a 6-well plate overnight prior to 24-hour treatment with 5μM SX-682. Cells were then lysed in a buffer containing 1% Triton X-100, 50mM HEPES, pH 7.4, 150mM NaCl, 1mM EGTA, 100mM NaF, 1.5mM $MgCl_2$, 10mM Na pyrophosphate, 1mM Na_3VO_4, 10% glycerol, and freshly added protease inhibitors (Cat# 05056489001, Roche) and phosphatase inhibitors (Cat# 04906837001, Roche) in 2mL reinforced tubes (Cat# P000943-LYSKO-A, Precellys). The homogenization sets at 5000 and goes for 10 sec for cells and 30 sec for tissue in the Precellys 24 Tissue Homogenizer. Lysates were centrifuged at 14,000rpm, 4°C for 2 minutes, and supernatants were collected. Protein concentration was adjusted to 1.5mg/mL and samples were stored in sample buffer (40% glycerol, 8% SDS, 0.25M Tris-HCL, pH 6.8. 10% β-mercaptoethanol is added just before use.) Samples were stored at -80°C until they were submitted to MD Anderson Cancer Center for processing and RPPA analysis of 480 proteins.

RPPA data were normalized and analyzed after a log2 transformation. All comparisons were performed using Welch's t-test. Changes in protein expression were considered significant based upon two criteria: p-value < 0.05 and a log_2(fold change) of ±2 (equivalent to a fold change of ±4). Functional protein association networks are presented using STRING version 11.5.

Statistical analysis

Data were summarized in figures using either the mean ± standard deviation (SD) for error bar charts or median with the first and third quartiles for boxplots. The mean of two groups were compared using Welch's t-test. For a comparison of more than two group means, the one-way analysis of variance (ANOVA) with post-hoc Tukey's test was used. The mean difference between two groups by the other factor was assessed in the context of a two-way ANOVA. Pairwise differences between two groups were compared using model-based mean comparisons. The Benjamini and Hochberg (BH) was used to adjust p-value for multiple comparisons as noted in the text to control the within experiment false discovery rate to less than 5%. Data was analyzed on a natural log scale or rank-based scales to meet the normality assumptions of statistical tests as needed. Survival curves are estimated using the Kaplan-Meier method and compared between two groups using the log-rank test. Levels of statistical significance are denoted * for $p<0.05$, ** for $p<0.01$, and *** for $p<0.001$, respectively. The analyses were performed using R version 4.1.2 or GraphPad Prism software. WGCNA statistical analysis was performed as described in the WGCNA methods.

References:

Addison, C.L., Daniel, T.O., Burdick, M.D., Liu, H., Ehlert, J.E., Xue, Y.Y., Buechi, L., Walz, A., Richmond, A., and Strieter, R.M. (2000). The CXC chemokine receptor 2, CXCR2, is the putative receptor for ELR+ CXC chemokine-induced angiogenic activity. J Immunol *165*, 5269-5277. 10.4049/jimmunol.165.9.5269.

Araki, S., Omori, Y., Lyn, D., Singh, R.K., Meinbach, D.M., Sandman, Y., Lokeshwar, V.B., and Lokeshwar, B.L. (2007). Interleukin-8 is a molecular determinant of androgen independence and progression in prostate cancer. Cancer Res *67*, 6854-6862. 10.1158/0008-5472.CAN-07-1162.

Balasoiu, M., Balasoiu, A.T., Mogoanta, S.S., Barbalan, A., Stepan, A.E., Ciurea, R.N., Alexandru, D.O., Enescu, A., and Mogoanta, L. (2014). Serum and tumor microenvironment IL-8 values in different stages of colorectal cancer. Rom J Morphol Embryol *55*, 575-578.

Balentien, E., Mufson, B.E., Shattuck, R.L., Derynck, R., and Richmond, A. (1991). Effects of MGSA/GRO alpha on melanocyte transformation. Oncogene *6*, 1115-1124.

Bennett, D.C., Cooper, P.J., and Hart, I.R. (1987). A line of non-tumorigenic mouse melanocytes, syngeneic with the B16 melanoma and requiring a tumour promoter for growth. Int J Cancer *39*, 414-418. 10.1002/ijc.2910390324.

Bertini, R., Allegretti, M., Bizzarri, C., Moriconi, A., Locati, M., Zampella, G., Cervellera, M.N., Di Cioccio, V., Cesta, M.C., Galliera, E., et al. (2004). Noncompetitive allosteric inhibitors of the inflammatory chemokine receptors CXCR1 and CXCR2: prevention of reperfusion injury. Proc Natl Acad Sci U S A *101*, 11791-11796. 10.1073/pnas.0402090101.

Bullock, K., and Richmond, A. (2021). Suppressing MDSC Recruitment to the Tumor Microenvironment by Antagonizing CXCR2 to Enhance the Efficacy of Immunotherapy. Cancers (Basel) *13*. 10.3390/cancers13246293.

Burd, C.E., Liu, W., Huynh, M.V., Waqas, M.A., Gillahan, J.E., Clark, K.S., Fu, K., Martin, B.L., Jeck, W.R., Souroullas, G.P., et al. (2014). Mutation-specific RAS oncogenicity explains NRAS codon 61 selection in melanoma. Cancer Discov *4*, 1418-1429. 10.1158/2159-8290.CD-14-0729.

Casilli, F., Bianchini, A., Gloaguen, I., Biordi, L., Alesse, E., Festuccia, C., Cavalieri, B., Strippoli, R., Cervellera, M.N., Di Bitondo, R., et al. (2005). Inhibition of interleukin-8 (CXCL8/IL-8) responses by repertaxin, a new inhibitor of the chemokine receptors CXCR1 and CXCR2. Biochem Pharmacol *69*, 385-394. 10.1016/j.bcp.2004.10.007.

Chapman, R.W., Phillips, J.E., Hipkin, R.W., Curran, A.K., Lundell, D., and Fine, J.S. (2009). CXCR2 antagonists for the treatment of pulmonary disease. Pharmacol Ther *121*, 55-68. 10.1016/j.pharmthera.2008.10.005.

Charafe-Jauffret, E., Ginestier, C., Iovino, F., Wicinski, J., Cervera, N., Finetti, P., Hur, M.H., Diebel, M.E., Monville, F., Dutcher, J., et al. (2009). Breast cancer cell lines contain functional cancer stem cells with metastatic capacity and a distinct molecular signature. Cancer Res *69*, 1302-1313. 10.1158/0008-5472.CAN-08-2741.

Che, J., Song, R., Chen, B., and Dong, X. (2020). Targeting CXCR1/2: The medicinal potential as cancer immunotherapy agents, antagonists research highlights and challenges ahead. Eur J Med Chem *185*, 111853. 10.1016/j.ejmech.2019.111853.

Cheng, Y., Mo, F., Li, Q., Han, X., Shi, H., Chen, S., Wei, Y., and Wei, X. (2021). Targeting CXCR2 inhibits the progression of lung cancer and promotes therapeutic effect of cisplatin. Mol Cancer *20*, 62. 10.1186/s12943-021-01355-1.

Dankort, D., Curley, D.P., Cartlidge, R.A., Nelson, B., Karnezis, A.N., Damsky, W.E., Jr., You, M.J., DePinho, R.A., McMahon, M., and Bosenberg, M. (2009). Braf(V600E) cooperates with Pten loss to induce metastatic melanoma. Nat Genet *41*, 544-552. 10.1038/ng.356.

Dankort, D., Filenova, E., Collado, M., Serrano, M., Jones, K., and McMahon, M. (2007). A new mouse model to explore the initiation, progression, and therapy of BRAFV600E-induced lung tumors. Genes Dev *21*, 379-384. 10.1101/gad.1516407.

Eikenberry, S., Thalhauser, C., and Kuang, Y. (2009). Tumor-immune interaction, surgical treatment, and cancer recurrence in a mathematical model of melanoma. PLoS Comput Biol *5*, e1000362. 10.1371/journal.pcbi.1000362.

Fan X, Patera AC, Pong-Kennedy A, Deno G, Gonsiorek W, Manfra DJ, Vassileva G, Zeng M, Jackson C, Sullivan L, Sharif-Rodriguez W, Opdenakker G, Van Damme J, Hedrick JA, Lundell D, Lira SA, Hipkin RW.J (2006). Murine CXCR1 is a functional receptor for GCP-2/CXCL6 and interleukin-8/CXCL8. J Biol Chem. 282:11658-66. doi: 10.1074/jbc.M607705200.

Feng, J.Liu T Qin B, Zhang Y, Liu XS (2012). Identifying ChIP-seq enrichment using MACS. *Nature protocols*7(9):1728-1740. 10.1002/0471250953.bi0214s34.

Feng, J., Liu, T. and Zhang, Y. Using MACS to identify peaks from ChIP-Seq data. (2011). *Current protocols in bioinformatics.* Chapter 2:Unit 2 14. 10.1002/0471250953.bi0214s34.

Fu J, Li K, Zhang W, Wan C, Zhang J, Jiang P, Liu XS. (2020). Large-scale public data reuse to model immunotherapy response and resistance. Genome Med 12:21 10.1186/s13073-020-0721-z.

Ginestier, C., Liu, S., Diebel, M.E., Korkaya, H., Luo, M., Brown, M., Wicinski, J., Cabaud, O., Charafe-Jauffret, E., Birnbaum, D., et al. (2010). CXCR1 blockade selectively targets human breast cancer stem cells in vitro and in xenografts. J Clin Invest *120*, 485-497. 10.1172/JCI39397.

Goto, Y., Yajima, I., Kumasaka, M., Ohgami, N., Tanaka, A., Tsuzuki, T., Inoue, Y., Fukushima, S., Ihn, H., Kyoya, M., et al. (2016). Transcription factor LSF (TFCP2) inhibits melanoma growth. Oncotarget 7, 2379-2390. 10.18632/oncotarget.6230

Ha, H., Debnath, B., and Neamati, N. (2017). Role of the CXCL8-CXCR1/2 Axis in Cancer and Inflammatory Diseases. Theranostics *7*, 1543-1588. 10.7150/thno.15625.

Hanahan, D. (2022). Hallmarks of Cancer: New Dimensions. Cancer Discov *12*, 31-46. 10.1158/2159-8290.CD-21-1059.

Hou, Y., Wu, Y., Farooq, S.M., Guan, X., Wang, S., Liu, Y., Oblak, J.J., Holcomb, J., Jiang, Y., Strieter, R.M., et al. (2015). A critical role of CXCR2 PDZ-mediated interactions in endothelial progenitor cell homing and angiogenesis. Stem Cell Res *14*, 133-143. 10.1016/j.scr.2014.12.001.

Hunt, F., Austin, C., Austin, R., Bonnert, R., Cage, P., Christie, J., Christie, M., Dixon, C., Hill, S., Jewell, R., et al. (2007). SAR studies on thiazolo[4,5-d]pyrimidine based CXCR2 antagonists involving a novel tandem displacement reaction. Bioorg Med Chem Lett *17*, 2731-2734. 10.1016/j.bmcl.2007.02.080.

Jiang P, Gu S, Pan D, Fu J, Sahu A, Hu X, Li Z, Traugh N, Bu X, Li B, et al: (2018). Signatures of T cell dysfunction and exclusion predict cancer immunotherapy response. Nat Med 24:1550-1558. 10.1038/s41591-018-0136-1.

Jung, J.H., Kang, K.W., Kim, J., Hong, S.C., Park, Y., and Kim, B.S. (2016). CXCR2 Inhibition in Human Pluripotent Stem Cells Induces Predominant Differentiation to Mesoderm and Endoderm Through Repression of mTOR, beta-Catenin, and hTERT Activities. Stem Cells Dev *25*, 1006-1019. 10.1089/scd.2015.0395.

Karras, P., Bordeu, I., Pozniak, J., Nowosad, A., Pazzi, C., Van Raemdonck, N., Landeloos, E., Van Herck, Y., Pedri, D., Bervoets, G., et al. (2022). A cellular hierarchy in melanoma uncouples growth and metastasis. Nature *610*, 190-198. 10.1038/s41586-022-05242-7.

Kotarba, G., Krzywinska, E., Grabowska, A.I., Taracha, A., and Wilanowski, T. (2018). TFCP2/TFCP2L1/UBP1 transcription factors in cancer. Cancer Lett 420, 72-79. 10.1016/j.canlet.2018.01.078.

Krausgruber T, Fortelny N, Fife-Gernedl V, Senekowitsch M, Schuster LC, Lercher A, Nemc A, Schmidl C, Rendeiro AF, Bergthaler A, and Bock C. (2020) Structural cells are key regulators of organ-specific immune responses. Nature. 583(7815):296-302. 10.1038/s41586-020-2424-4.

Langfelder P and Horvath S (2008). WGCNA: an R package for weighted correlation network analysis. BMC Bioinformatics. 9:559. 10.1186/1471-2105-9-559

Langmead, B. and Salzberg, S.L. Fast gapped-read alignment with Bowtie 2. Nat Methods 2012;9(4):357-359. 10.1038/nmeth.1923.

Larribere, L., and Utikal, J. (2014). De- and re-differentiation of the melanocytic lineage. Eur J Cell Biol *93*, 30-35. 10.1016/j.ejcb.2013.11.006.

Leaker, B.R., Barnes, P.J., and O'Connor, B. (2013). Inhibition of LPS-induced airway neutrophilic inflammation in healthy volunteers with an oral CXCR2 antagonist. Respir Res *14*, 137. 10.1186/1465-9921-14-137.

Li M, Luo X, Meng Y, Mei J, Zhu X, Jin L, Li D. (2012). CXCL8 enhances proliferation and growth and reduces apoptosis in endometrial stromal cells in an autocrine manner via a CXCR1-triggered PTEN/AKT signal pathway. Hum Reprod. 27: 2107-2116. 10.1093/humrep/des132.

Liao, W., Overman, M.J., Boutin, A.T., Shang, X., Zhao, D., Dey, P., Li, J., Wang, G., Lan, Z., Li, J., et al. (2019). KRAS-IRF2 Axis Drives Immune Suppression and Immune

Therapy Resistance in Colorectal Cancer. Cancer Cell *35*, 559-572 e557. 10.1016/j.ccell.2019.02.008.

Liu, D., Schilling, B., Liu, D., Sucker, A., Livingstone, E., Jerby-Arnon, L., Zimmer, L., Gutzmer, R., Satzger, I., Loquai, C., et al. (2019a). Integrative molecular and clinical modeling of clinical outcomes to PD1 blockade in patients with metastatic melanoma. Nat Med *25*, 1916-1927. 10.1038/s41591-019-0654-5.

Liu, G., An, L., Zhang, H., Du, P., and Sheng, Y. (2019b). Activation of CXCL6/CXCR1/2 Axis Promotes the Growth and Metastasis of Osteosarcoma Cells in vitro and in vivo. Front Pharmacol *10*, 307. 10.3389/fphar.2019.00307.

Liu, K., Zhang, Y., Liu, D., Ying, Q.L., and Ye, S. (2017). TFCP2L1 represses multiple lineage commitment of mouse embryonic stem cells through MTA1 and LEF1. J Cell Sci *130*, 3809-3817. 10.1242/jcs.206532.

Liu, L., Li, M., Spangler, L.C., Spear, C., Veenstra, M., Darnall, L., Chang, C., Cotleur, A.C., and Ransohoff, R.M. (2013). Functional defect of peripheral neutrophils in mice with induced deletion of CXCR2. Genesis *51*, 587-595. 10.1002/dvg.22401.

Love MI, Huber W, Anders S. (2014). Moderated estimation of fold change and dispersion for RNA-seq data with DESeq2. Genome Biol 15:550. 10.1186/x13059-014-0550-8.

Luan, J., Shattuck-Brandt, R., Haghnegahdar, H., Owen, J.D., Strieter, R., Burdick, M., Nirodi, C., Beauchamp, D., Johnson, K.N., and Richmond, A. (1997). Mechanism and biological significance of constitutive expression of MGSA/GRO chemokines in malignant melanoma tumor progression. J Leukoc Biol *62*, 588-597. 10.1002/jlb.62.5.588.

Maeda, D.Y., Peck, A.M., Schuler, A.D., Quinn, M.T., Kirpotina, L.N., Wicomb, W.N., Fan, G.H., and Zebala, J.A. (2014). Discovery of 2-[5-(4-Fluorophenylcarbamoyl)pyridin-2-ylsulfanylmethyl]phenylboronic Acid (SX-517): Noncompetitive Boronic Acid Antagonist of CXCR1 and CXCR2. J Med Chem *57*, 8378-8397. 10.1021/jm500827t.

Maeda, D.Y., Quinn, M.T., Schepetkin, I.A., Kirpotina, L.N., and Zebala, J.A. (2010). Nicotinamide glycolates antagonize CXCR2 activity through an intracellular mechanism. J Pharmacol Exp Ther *332*, 145-152. 10.1124/jpet.109.159020.

Matsushima, K., Yang, and Oppenheim, J.J. (2022). Interleukin-8: An evolving chemokine. Cytokine *153*, 155828. 10.1016/j.cyto.2022.155828.

Mica, Y., Lee, G., Chambers, S.M., Tomishima, M.J., and Studer, L. (2013). Modeling neural crest induction, melanocyte specification, and disease-related pigmentation defects in hESCs and patient-specific iPSCs. Cell Rep *3*, 1140-1152. 10.1016/j.celrep.2013.03.025.

Moepps B, Nuesseler E, Braun M, Gierschik P (2006). A homolog of the human chemokine receptor CXCR1 is expressed in the mouse. Mol Immunol. 43:897-914. 10.1016/j.molimm.2005.06.043.

Moepps B (2015). CXCR1 and CXCR2 and Ligands. Encyclopedia of Inflammatory Diseases. pp 1-10. Birkhäuser, Basel. https://doi.org/10.1007/978-3-0348-0620-6_223-1

Moser, B. (2022). Emerging Roles of Chemokines in Cancer Immunotherapy. Cancers (Basel) *14*. 10.3390/cancers14153593.

Muzumdar, M.D., Tasic, B., Miyamichi, K., Li, L., and Luo, L. (2007). A global double-fluorescent Cre reporter mouse. Genesis *45*, 593-605. 10.1002/dvg.20335.

Ouyang Z, Zhou Q, Wong W H, (2009). ChIP-seq of transcription factors predicts absolute and differential gene expression in embryonic stem cells. Proc Natl. Acad Sci, USA. 106: 21521-21526. 10.1073/pnas.0904863106. .

Park, G.Y., Pathak, H.B., Godwin, A.K., and Kwon, Y. (2021). Epithelial-stromal communication via CXCL1-CXCR2 interaction stimulates growth of ovarian cancer cells through p38 activation. Cell Oncol (Dordr) *44*, 77-92. 10.1007/s13402-020-00554-0.

Petitprez, F., Levy, S., Sun, C.M., Meylan, M., Linhard, C., Becht, E., Elarouci, N., Tavel, D., Roumenina, L.T., Ayadi, M., et al. (2020). The murine Microenvironment Cell Population counter method to estimate abundance of tissue-infiltrating immune and stromal cell populations in murine samples using gene expression. Genome Med *12*, 86. 10.1186/s13073-020-00783-w.

Pine, S.R., Mechanic, L.E., Enewold, L., Chaturvedi, A.K., Katki, H.A., Zheng, Y.L., Bowman, E.D., Engels, E.A., Caporaso, N.E., and Harris, C.C. (2011). Increased levels of circulating interleukin 6, interleukin 8, C-reactive protein, and risk of lung cancer. J Natl Cancer Inst *103*, 1112-1122. 10.1093/jnci/djr216.

Qiu, D., Ye, S., Ruiz, B., Zhou, X., Liu, D., Zhang, Q., and Ying, Q.L. (2015). Klf2 and Tfcp2l1, Two Wnt/beta-Catenin Targets, Act Synergistically to Induce and Maintain Naive Pluripotency. Stem Cell Reports *5*, 314-322. 10.1016/j.stemcr.2015.07.014.

Raman, D., Baugher, P.J., Thu, Y.M., and Richmond, A. (2007). Role of chemokines in tumor growth. Cancer Lett *256*, 137-165. 10.1016/j.canlet.2007.05.013.

Raman D, Sobolik-Delmaire T, Richmond A. (2011). Chemokines in health and disease. Exp Cell Res. 317:575-589. 10.1016/j.yexcr.2011.01.005

Riaz, N., Havel, J.J., Makarov, V., Desrichard, A., Urba, W.J., Sims, J.S., Hodi, F.S., Martin-Algarra, S., Mandal, R., Sharfman, W.H., et al. (2017). Tumor and Microenvironment Evolution during Immunotherapy with Nivolumab. Cell *171*, 934-949 e916. 10.1016/j.cell.2017.09.028.

Richmond, A., Balentien, E., Thomas, H.G., Flaggs, G., Barton, D.E., Spiess, J., Bordoni, R., Francke, U., and Derynck, R. (1988). Molecular characterization and chromosomal mapping of melanoma growth stimulatory activity, a growth factor structurally related to beta-thromboglobulin. EMBO J *7*, 2025-2033. 10.1002/j.1460-2075.1988.tb03042.x.

Richmond, A., Fan, G.H., Dhawan, P., and Yang, J. (2004). How do chemokine/chemokine receptor activations affect tumorigenesis? Novartis Found Symp *256*, 74-89; discussion 89-91, 106-111, 266-109.

Richmond, A., Yang, J., and Su, Y. (2009). The good and the bad of chemokines/chemokine receptors in melanoma. Pigment Cell Melanoma Res *22*, 175-186. 10.1111/j.1755-148X.2009.00554.x.

Romero-Moreno, R., Curtis, K.J., Coughlin, T.R., Miranda-Vergara, M.C., Dutta, S., Natarajan, A., Facchine, B.A., Jackson, K.M., Nystrom, L., Li, J., et al. (2019). The CXCL5/CXCR2 axis is sufficient to promote breast cancer colonization during bone metastasis. Nat Commun *10*, 4404. 10.1038/s41467-019-12108-6.

Ruffini, P.A. (2019). The CXCL8-CXCR1/2 Axis as a Therapeutic Target in Breast Cancer Stem-Like Cells. Front Oncol *9*, 40. 10.3389/fonc.2019.00040.

Sai, J., Raman, D., Liu, Y., Wikswo, J., and Richmond, A. (2008). Parallel phosphatidylinositol 3-kinase (PI3K)-dependent and Src-dependent pathways lead to CXCL8-mediated Rac2 activation and chemotaxis. J Biol Chem *283*, 26538-26547. 10.1074/jbc.M805611200.

Schott, A.F., Goldstein, L.J., Cristofanilli, M., Ruffini, P.A., McCanna, S., Reuben, J.M., Perez, R.P., Kato, G., and Wicha, M. (2017). Phase Ib Pilot Study to Evaluate Reparixin in Combination with Weekly Paclitaxel in Patients with HER-2-Negative Metastatic Breast Cancer. Clin Cancer Res *23*, 5358-5365. 10.1158/1078-0432.CCR-16-2748.

Shang, F.M., and Li, J. (2019). A small-molecule antagonist of CXCR1 and CXCR2 inhibits cell proliferation, migration and invasion in melanoma via PI3K/AKT pathway. Med Clin (Barc) *152*, 425-430. 10.1016/j.medcli.2018.08.006.

Shi, Z., Yang, W.M., Chen, L.P., Yang, D.H., Zhou, Q., Zhu, J., Chen, J.J., Huang, R.C., Chen, Z.S., and Huang, R.P. (2012). Enhanced chemosensitization in multidrug-resistant human breast cancer cells by inhibition of IL-6 and IL-8 production. Breast Cancer Res Treat *135*, 737-747. 10.1007/s10549-012-2196-0.

Singh, J.K., Farnie, G., Bundred, N.J., Simoes, B.M., Shergill, A., Landberg, G., Howell, S.J., and Clarke, R.B. (2013). Targeting CXCR1/2 significantly reduces breast cancer stem cell activity and increases the efficacy of inhibiting HER2 via HER2-dependent and -independent mechanisms. Clin Cancer Res *19*, 643-656. 10.1158/1078-0432.CCR-12-1063.

Singh, S., Nannuru, K.C., Sadanandam, A., Varney, M.L., and Singh, R.K. (2009a). CXCR1 and CXCR2 enhances human melanoma tumourigenesis, growth and invasion. Br J Cancer *100*, 1638-1646. 10.1038/sj.bjc.6605055.

Singh, S., Sadanandam, A., and Singh, R.K. (2007). Chemokines in tumor angiogenesis and metastasis. Cancer Metastasis Rev *26*, 453-467. 10.1007/s10555-007-9068-9.

Singh, S., Sadanandam, A., Varney, M.L., Nannuru, K.C., and Singh, R.K. (2010). Small interfering RNA-mediated CXCR1 or CXCR2 knock-down inhibits melanoma tumor growth and invasion. Int J Cancer *126*, 328-336. 10.1002/ijc.24714.

Singh, S., Varney, M., and Singh, R.K. (2009b). Host CXCR2-dependent regulation of melanoma growth, angiogenesis, and experimental lung metastasis. Cancer Res *69*, 411-415. 10.1158/0008-5472.CAN-08-3378.

Souza, D.G., Bertini, R., Vieira, A.T., Cunha, F.Q., Poole, S., Allegretti, M., Colotta, F., and Teixeira, M.M. (2004). Repertaxin, a novel inhibitor of rat CXCR2 function, inhibits inflammatory responses that follow intestinal ischaemia and reperfusion injury. Br J Pharmacol *143*, 132-142. 10.1038/sj.bjp.0705862.

Sun, H., You, Y., Guo, M., Wang, X., Zhang, Y., and Ye, S. (2018). Tfcp2l1 safeguards the maintenance of human embryonic stem cell self-renewal. J Cell Physiol *233*, 6944-6951. 10.1002/jcp.26483.

Sun, L., Clavijo, P.E., Robbins, Y., Patel, P., Friedman, J., Greene, S., Das, R., Silvin, C., Van Waes, C., Horn, L.A., et al. (2019). Inhibiting myeloid-derived suppressor cell trafficking enhances T cell immunotherapy. JCI Insight *4*. 10.1172/jci.insight.126853.

Takashima, Y., Guo, G., Loos, R., Nichols, J., Ficz, G., Krueger, F., Oxley, D., Santos, F., Clarke, J., Mansfield, W., et al. (2014). Resetting transcription factor control circuitry toward ground-state pluripotency in human. Cell *158*, 1254-1269. 10.1016/j.cell.2014.08.029.

Utikal, J., Maherali, N., Kulalert, W., and Hochedlinger, K. (2009). Sox2 is dispensable for the reprogramming of melanocytes and melanoma cells into induced pluripotent stem cells. J Cell Sci *122*, 3502-3510. 10.1242/jcs.054783.

Vandercappellen, J., Van Damme, J., and Struyf, S. (2008). The role of CXC chemokines and their receptors in cancer. Cancer Lett *267*, 226-244. 10.1016/j.canlet.2008.04.050.

Wang, X., Wang, X., Zhang, S., Sun, H., Li, S., Ding, H., You, Y., Zhang, X., and Ye, S.D. (2019). The transcription factor TFCP2L1 induces expression of distinct target genes and promotes self-renewal of mouse and human embryonic stem cells. J Biol Chem *294*, 6007-6016. 10.1074/jbc.RA118.006341.

Wilson, C., Wilson, T., Johnston, P.G., Longley, D.B., and Waugh, D.J. (2008). Interleukin-8 signaling attenuates TRAIL- and chemotherapy-induced apoptosis through transcriptional regulation of c-FLIP in prostate cancer cells. Mol Cancer Ther *7*, 2649-2661. 10.1158/1535-7163.MCT-08-0148.

Wooten DJ, Groves SM, Tyson DR, Liu Q, Lim JS, Albert R, Lopez CF, Sage J, Quaranta V. 2019. Systems-level network modeling of Small Cell Lung Cancer subtypes identifies master regulators and destabilizers. Plos Comput Biol 15: e1007343. https://journals.plos.org/ploscompbiol/article?id=10.1371/journal.pcbi.1007343.

Xu W, Ye Y, Sharrocks AD, Zhang W, Chen X (2020). Genome-wide interrogation of protein-DNA interactions in mammalian cells using ChIPmentation. STAR Protoc. 1(3):100187 10.1016/j.xpro.2020.100187

Yan C and Richmond A. (2021). Hiding in the dark: pan-cancer characterization of expression and clinical relevance of CD40 to immune checkpoint blockade therapy. Mol Cancer 20: 146, 10.1186/s12943-021-01442-3.

Yang, J., and Richmond, A. (2001). Constitutive IkappaB kinase activity correlates with nuclear factor-kappaB activation in human melanoma cells. Cancer Res *61*, 4901-4909.

Yang, J., Yan, C., Vilgelm, A.E., Chen, S.C., Ayers, G.D., Johnson, C.A., and Richmond, A. (2021). Targeted Deletion of CXCR2 in Myeloid Cells Alters the Tumor Immune Environment to Improve Antitumor Immunity. Cancer Immunol Res *9*, 200-213. 10.1158/2326-6066.CIR-20-0312.

Yang, J., Zaja-Milatovic, S., Thu, Y.M., Lee, F., Smykla, R., and Richmond, A. (2009). Molecular determinants of melanoma malignancy: selecting targets for improved efficacy of chemotherapy. Mol Cancer Ther *8*, 636-647. 1535-7163. MCT-08-0749 [pii]10.1158/1535-7163.MCT-08-0749.

Ye, S., Li, P., Tong, C., and Ying, Q.L. (2013). Embryonic stem cell self-renewal pathways converge on the transcription factor Tfcp2l1. EMBO J *32*, 2548-2560. 10.1038/emboj.2013.175.

Yoganandarajah, V., Patel, J., van Schaijik, B., Bockett, N., Brasch, H.D., Paterson, E., Sim, D., Davis, P.F., Roth, I.M., Itinteang, T., and Tan, S.T. (2020). Identification of Cancer Stem Cell Subpopulations in Head and Neck Metastatic Malignant Melanoma. Cells *9*. 10.3390/cells9020324.

Zabierowski, S.E., and Herlyn, M. (2010). Embryonic stem cells as a model for studying melanocyte development. Methods Mol Biol *584*, 301-316. 10.1007/978-1-60761-369-5_16.

Zhang, M., Ji, J., Wang, X., Zhang, X., Zhang, Y., Li, Y., Wang, X., Li, X., Ban, Q., and Ye, S.D. (2021). The transcription factor Tfcp2l1 promotes primordial germ cell-like cell specification of pluripotent stem cells. J Biol Chem *297*, 101217. 10.1016/j.jbc.2021.101217.

Zhang, Y., Liu T, Meyer CA, Eeckhoute J, Johnson DS, Bernstein BE, Nusbaum C, Meyers RM, Brown M, Li W, Siu S. Model-based analysis of ChIP-Seq (MACS). *Genome biology* 2008;9(9):R137. 10.1186/gb-2008-9-9-r137

Zhou Y, Zhou B, Pache L, Chang M, Khodabakhshi A H, Tanaseichuk O, Benner C, Chanda SK. (2019). Metascape provides a biologist-oriented resource for the analysis of systems-level datasets. Nature Commun. 10: 1523-1563. 10.1038/s41467-019-09234-6.

Figure 1.

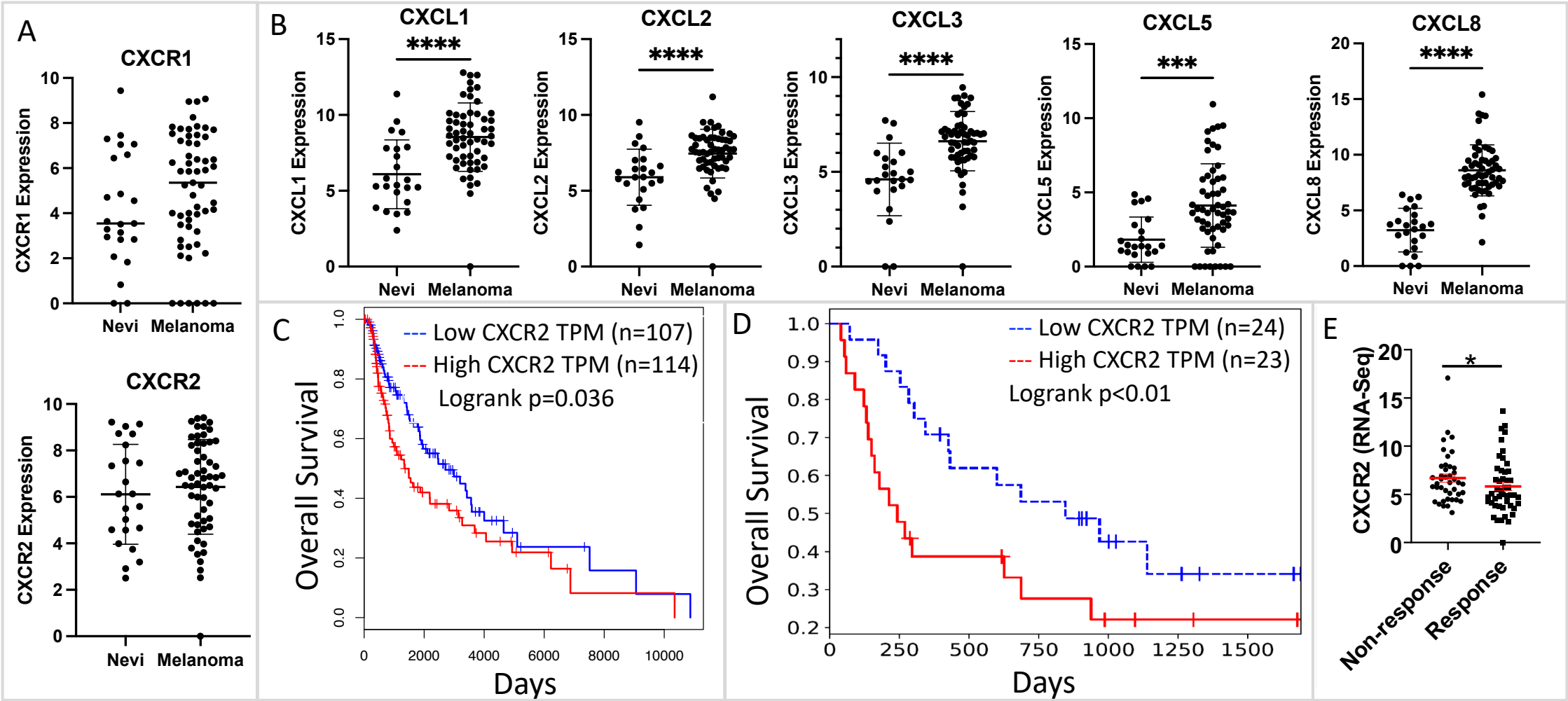
A
CXCR1
CXCR1 Expression
Nevi
Melanoma
CXCR2
CXCR2 Expression
B
CXCL1
CXCL1 Expression
****
CXCL2
CXCL2 Expression
****
CXCL3
CXCL3 Expression
****
CXCL5
CXCL5 Expression
***
CXCL8
CXCL8 Expression
****
C
Low CXCR2 TPM (n=107)
High CXCR2 TPM (n=114)
Logrank p=0.036
Overall Survival
Days
D
Low CXCR2 TPM (n=24)
High CXCR2 TPM (n=23)
Logrank p<0.01
Overall Survival
Days
E
CXCR2 (RNA-Seq)
*
Non-response
Response

Figure 2.

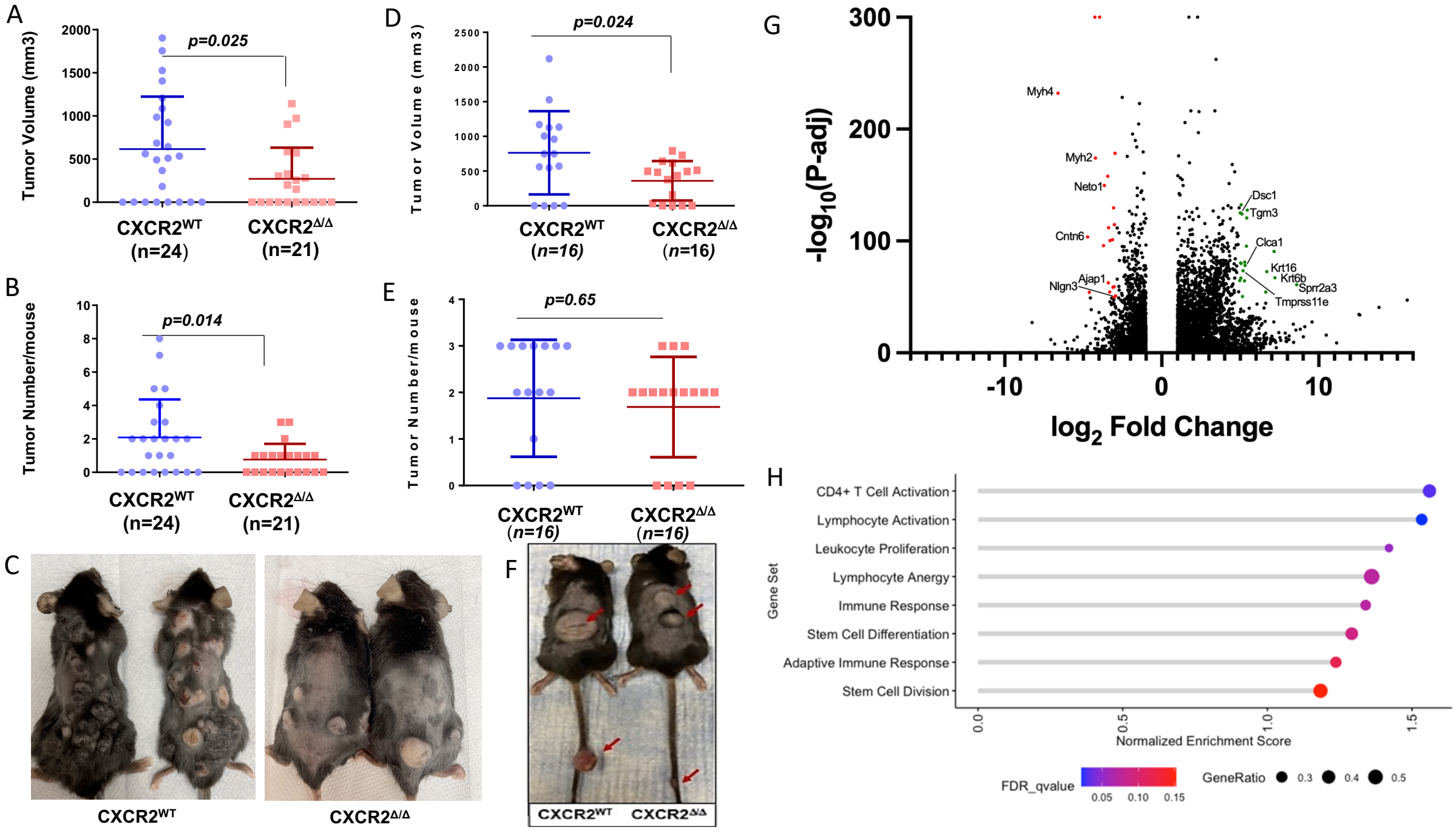
A
Tumor Volume (mm3)
p=0.025
CXCR2WT (n=24)
CXCR2Δ/Δ (n=21)
B
Tumor Number/mouse
p=0.014
CXCR2WT (n=24)
CXCR2Δ/Δ (n=21)
C
CXCR2WT
CXCR2Δ/Δ
D
Tumor Volume (mm3)
p=0.024
CXCR2WT (n=16)
CXCR2Δ/Δ (n=16)
E
Tumor Number/mouse
p=0.65
CXCR2WT (n=16)
CXCR2Δ/Δ (n=16)
F
CXCR2WT
CXCR2Δ/Δ
G
-log10(P-adj)
log2 Fold Change
Myh4
Myh2
Neto1
Cntn6
Ajap1
Nlgn3
Dsc1
Tgm3
Clca1
Krt16
Krt6b
Sprr2a3
Tmprss11e
H
Gene Set
CD4+ T Cell Activation
Lymphocyte Activation
Leukocyte Proliferation
Lymphocyte Anergy
Immune Response
Stem Cell Differentiation
Adaptive Immune Response
Stem Cell Division
Normalized Enrichment Score
FDR_qvalue
GeneRatio

Figure 3.

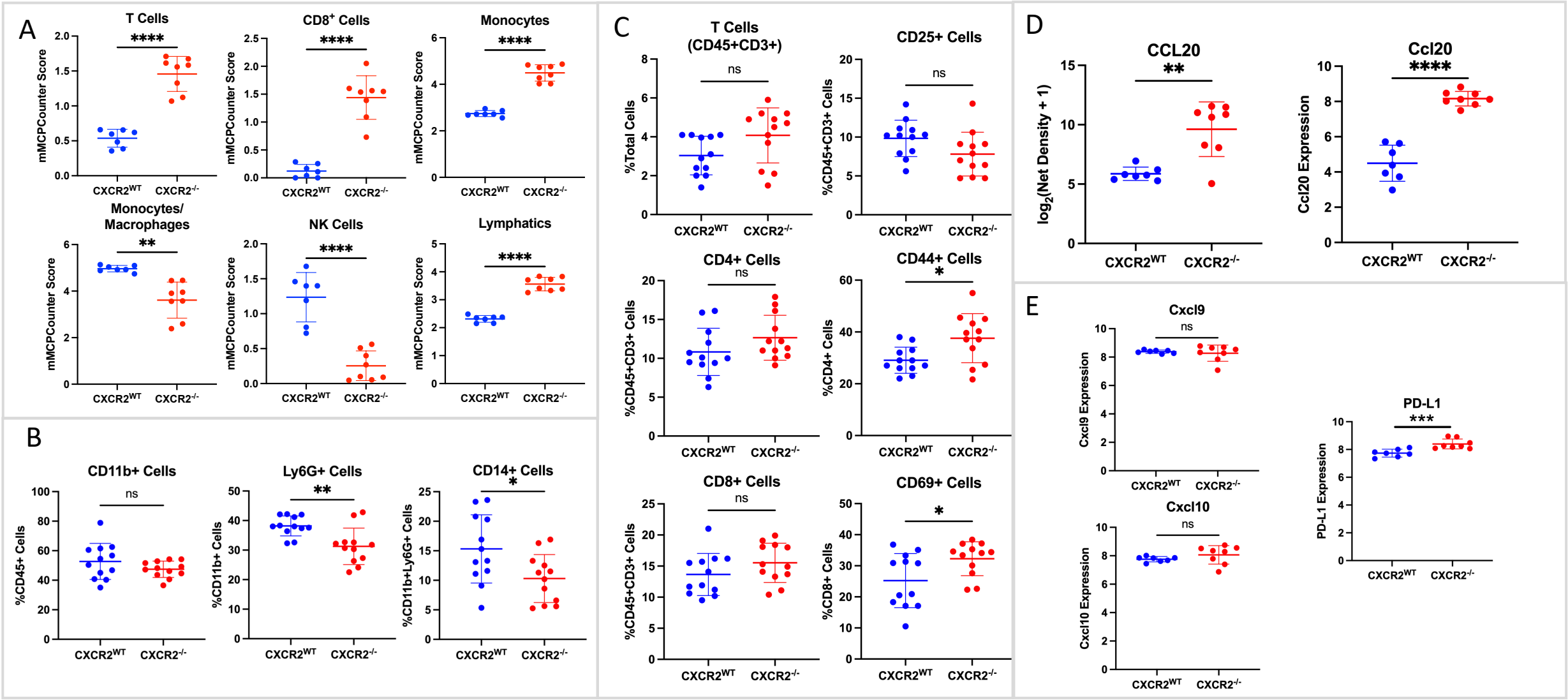
A
T Cells
****
mMCPCounter Score
CD8+ Cells
****
Monocytes
****
Monocytes/ Macrophages
**
NK Cells
****
Lymphatics
****
CXCR2WT
CXCR2-/-
B
CD11b+ Cells
ns
%CD45+ Cells
Ly6G+ Cells
**
%CD11b+ Cells
CD14+ Cells
*
%CD11b+Ly6G+ Cells
C
T Cells (CD45+CD3+)
ns
%Total Cells
CD25+ Cells
ns
%CD45+CD3+ Cells
CD4+ Cells
ns
CD44+ Cells
*
%CD4+ Cells
CD8+ Cells
ns
CD69+ Cells
*
%CD8+ Cells
D
CCL20
**
log2(Net Density + 1)
Ccl20
****
Ccl20 Expression
E
Cxcl9
ns
Cxcl9 Expression
PD-L1
***
PD-L1 Expression
Cxcl10
ns
Cxcl10 Expression

Figure 4.

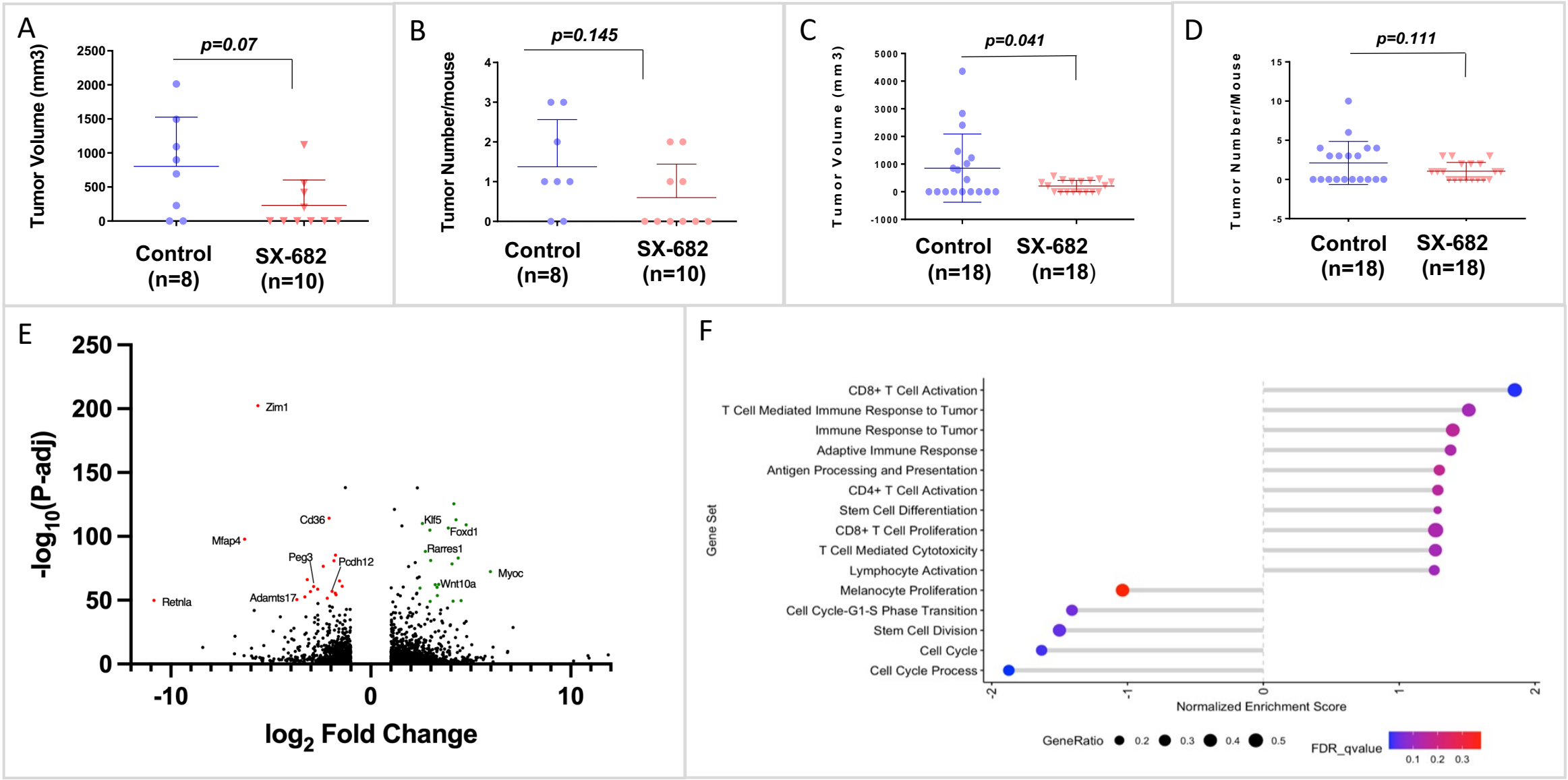
A
p=0.07
Tumor Volume (mm3)
2500
2000
1500
1000
500
0
Control (n=8)
SX-682 (n=10)
B
p=0.145
Tumor Number/mouse
4
3
2
1
0
Control (n=8)
SX-682 (n=10)
C
p=0.041
Tumor Volume (mm3)
5000
4000
3000
2000
1000
0
-1000
Control (n=18)
SX-682 (n=18)
D
p=0.111
Tumor Number/Mouse
15
10
5
0
-5
Control (n=18)
SX-682 (n=18)
E
-log10(P-adj)
250
200
150
100
50
0
Zim1
Cd36
Klf5
Foxd1
Mfap4
Rarres1
Peg3
Pcdh12
Myoc
Wnt10a
Adamts17
Retnla
-10
0
10
log2 Fold Change
F
Gene Set
CD8+ T Cell Activation
T Cell Mediated Immune Response to Tumor
Immune Response to Tumor
Adaptive Immune Response
Antigen Processing and Presentation
CD4+ T Cell Activation
Stem Cell Differentiation
CD8+ T Cell Proliferation
T Cell Mediated Cytotoxicity
Lymphocyte Activation
Melanocyte Proliferation
Cell Cycle-G1-S Phase Transition
Stem Cell Division
Cell Cycle
Cell Cycle Process
-2
-1
0
1
2
Normalized Enrichment Score
GeneRatio
0.2
0.3
0.4
0.5
FDR_qvalue
0.1
0.2
0.3

Figure 5.

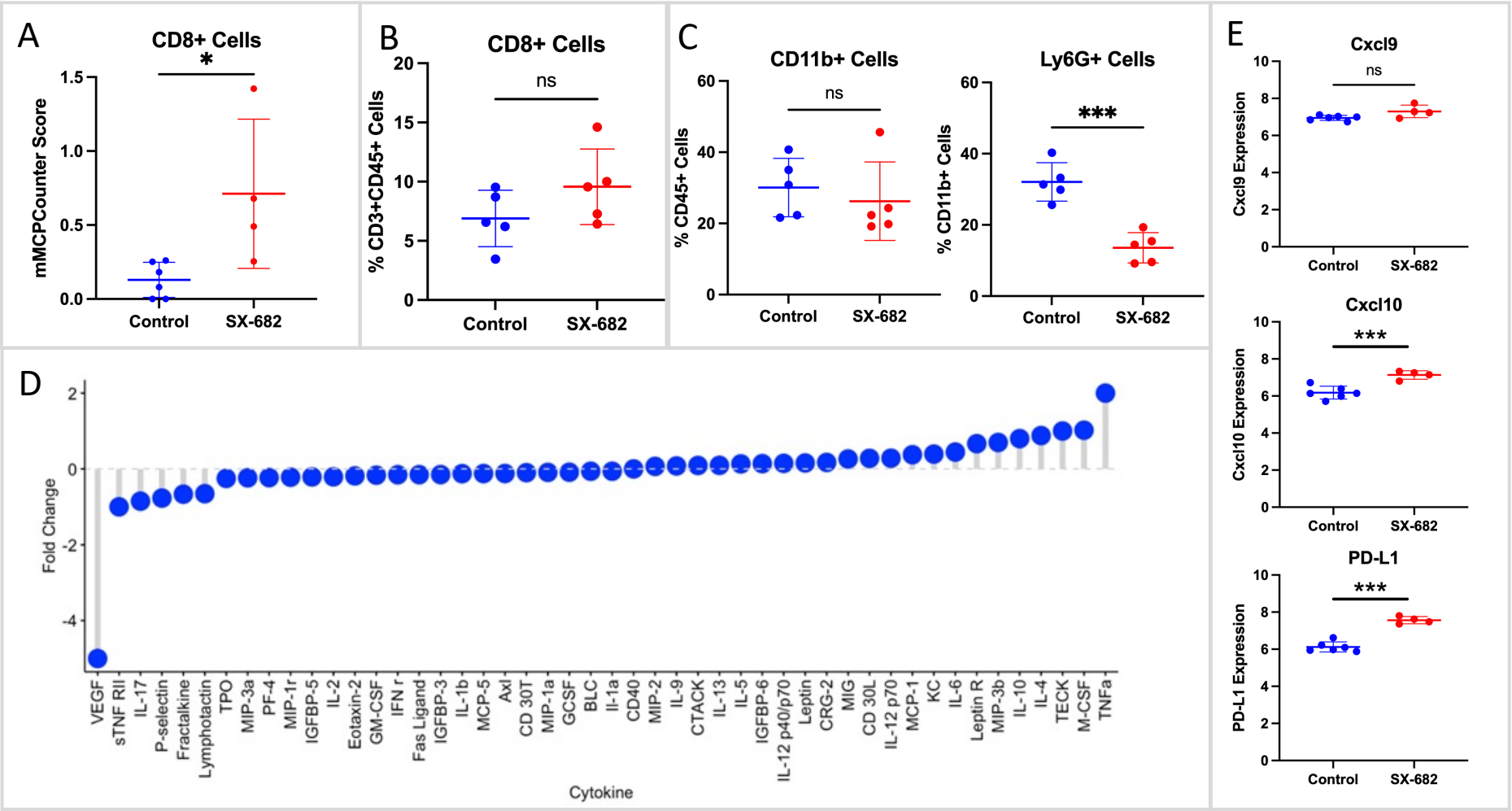
A
CD8+ Cells
*
mMCPCounter Score
1.5
1.0
0.5
0.0
Control
SX-682
B
CD8+ Cells
ns
% CD3+CD45+ Cells
20
15
10
5
0
Control
SX-682
C
CD11b+ Cells
ns
% CD45+ Cells
60
40
20
0
Control
SX-682
Ly6G+ Cells
***
% CD11b+ Cells
60
40
20
0
Control
SX-682
D
Fold Change
2
0
-2
-4
VEGF
sTNF RII
IL-17
P-selectin
Fractalkine
Lymphotactin
TPO
MIP-3a
PF-4
MIP-1r
IGFBP-5
IL-2
Eotaxin-2
GM-CSF
IFN r
Fas Ligand
IGFBP-3
IL-1b
MCP-5
Axl
CD 30T
MIP-1a
GCSF
BLC
Il-1a
CD40
MIP-2
IL-9
CTACK
IL-13
IL-5
IGFBP-6
IL-12 p40/p70
Leptin
CRG-2
MIG
CD 30L
IL-12 p70
MCP-1
KC
IL-6
Leptin R
MIP-3b
IL-10
IL-4
TECK
M-CSF
TNFa
Cytokine
E
Cxcl9
ns
Cxcl9 Expression
10
8
6
4
2
0
Control
SX-682
Cxcl10
***
Cxcl10 Expression
10
8
6
4
2
0
Control
SX-682
PD-L1
***
PD-L1 Expression
10
8
6
4
2
0
Control
SX-682

Figure 6.

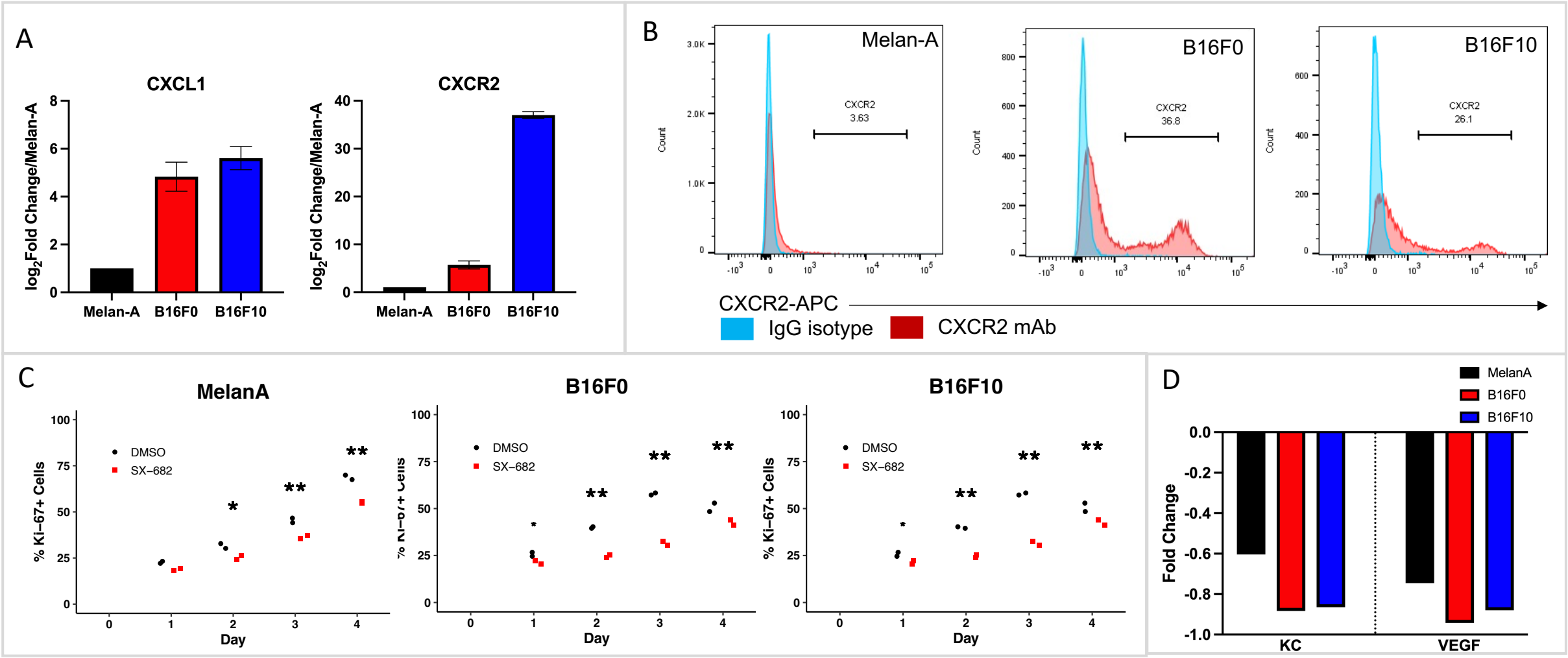
A
CXCL1
CXCR2
log2Fold Change/Melan-A
Melan-A
B16F0
B16F10
B
Melan-A
B16F0
B16F10
CXCR2
3.63
36.8
26.1
Count
CXCR2-APC
IgG isotype
CXCR2 mAb
C
MelanA
B16F0
B16F10
% Ki-67+ Cells
DMSO
SX-682
Day
D
MelanA
B16F0
B16F10
Fold Change
KC
VEGF

Figure 7.

A

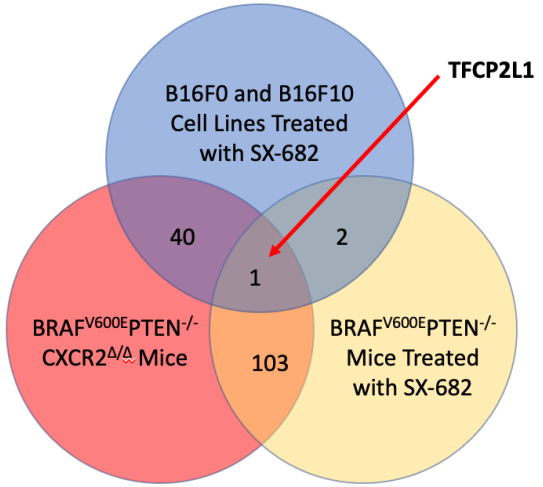

B

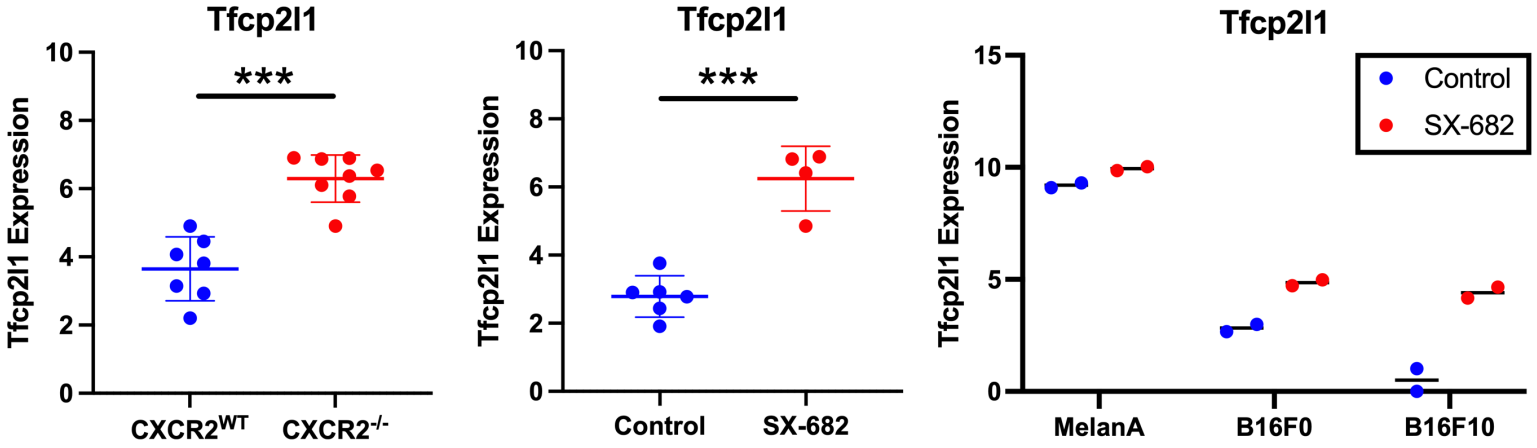

C

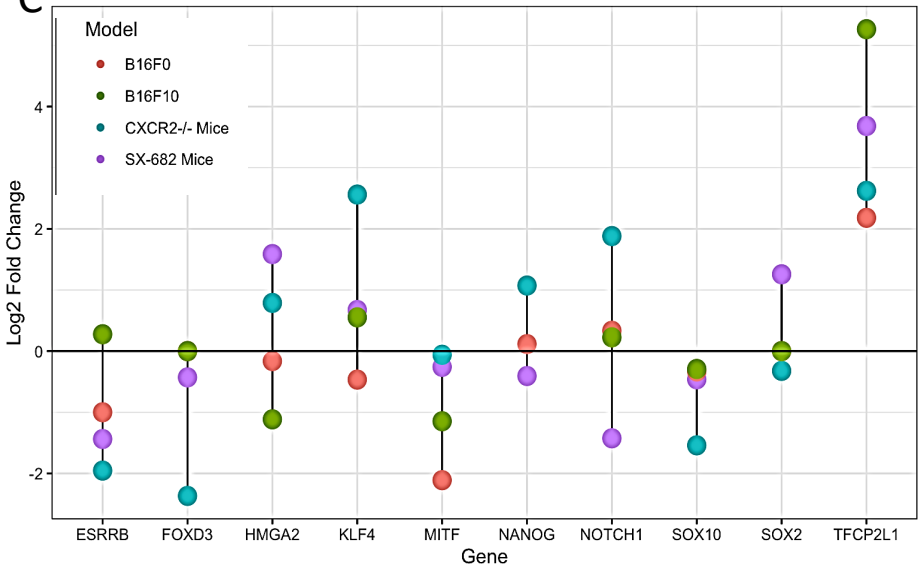

D

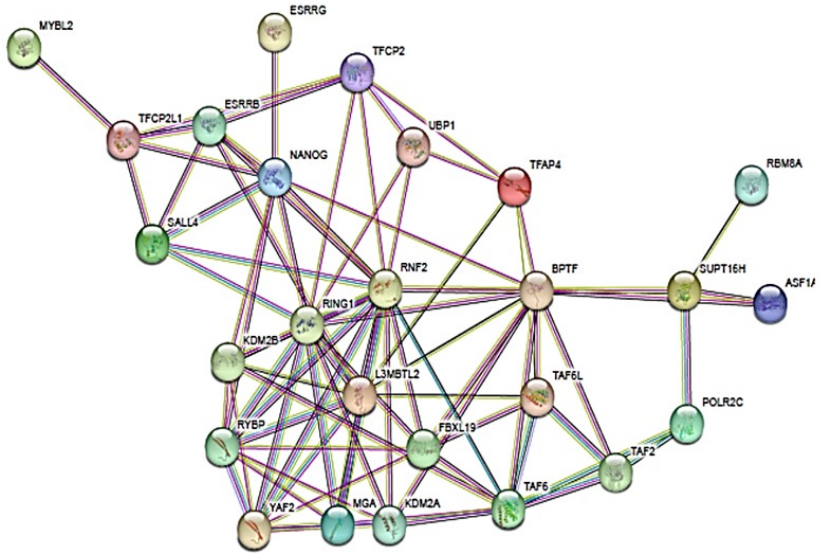
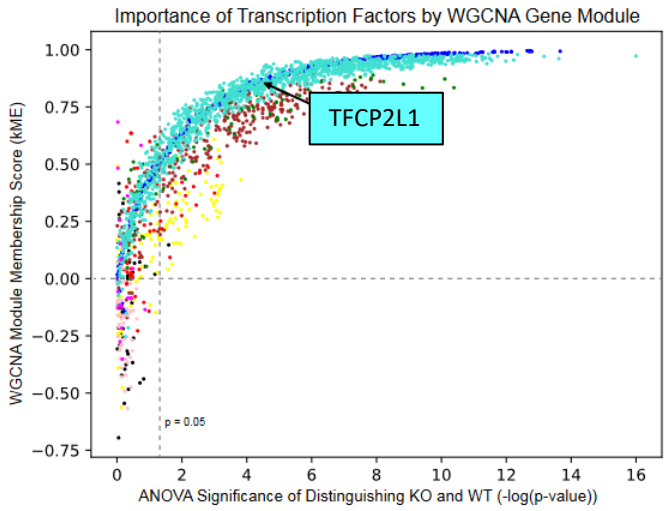
F